universität wien

MASTERARBEIT / MASTER'S THESIS

Titel der Masterarbeit / Title of the Master's Thesis

„CORROSION PROPERTIES OF BIODEGRADABLE SPD-PROCESSED AND THERMALLY TREATED Zn-Mg ALLOYS“

verfasst von / submitted by

Ruri LEE, BSc

angestrebter akademischer Grad / in partial fulfilment of the requirements for the degree of

Master of Science (MSc)

Wien, 2022 / Vienna 2022

Studienkennzahl lt. Studienblatt / degree programme code as it appears on the student record sheet:	UA 066 876
Studienrichtung lt. Studienblatt / degree programme as it appears on the student record sheet:	Physik / Physics
Betreut von / Supervisor:	Ao. Univ.-Prof. i.R. Dr. Michael Zehetbauer
Mitbetreut von / Co-Supervisor:	

Acknowledgments

„Streng dich an. Deine Mühen werden sich nämlich bezahlt machen.“

- Jongsoo LEE -

Firstly, I would like to express my sincere gratitude to my supervisor, Prof. Michael Zehetbauer, for his continuous support, guidance, patience, and warm encouragement throughout my research. Working on my master's thesis with a professor whom I admire was a great pleasure for me.

I would also like to express my deepest gratitude to Dr. Jelena Horky from the AIT Austria Institute of Technology. She was always sincerely encouraging and supportive of my efforts to complete this thesis. It would not have been possible to complete this work without her help and insightful comments. Also, my sincere thanks go to the AIT Health and Environment team in making my first internship in Austria a success with their encouraging words, support, and kindness.

I'd like to thank Dr. Bartosz Sulkowski of the Faculty of Non-Ferrous Metals at AGH University of Science and Technology in Krakow, Poland, for casting the alloys, and my colleague Lukas Aitzetmüller for further preparing of the samples studied in this thesis.

Sincere appreciation to FFG (Austrian Research Promotion Agency). I was supported financially by an FFG FEMtech Internship for Female Students, allowing me to focus entirely on my research during the course of this work.

My heartfelt gratitude goes to my friends; Yumi Kim, Doori Jung, Tobias Sammet, and Dr. Jooyoung Hahn, and very special thanks go to Sunah Kwak.

Last but not least, from the bottom of my heart, I would like to thank my parents Jongsoo Lee and Youngsoon You, and my brother Taewoong Lee for their endless love, prayers, and encouragement.

Abstract

Biodegradable metallic materials, such as iron, magnesium, and zinc, are attracting the increasing attention of many researchers as materials that can overcome the adverse effects of permanent materials for orthopedic implants and vascular stents. Recently, zinc and zinc-based alloys are suggested to be more promising candidates due to their proper biodegradability rate in the middle between those of iron and magnesium.

In this study, the corrosion behavior of two zinc-based binary alloys, containing 0.5 and 1 weight percent of magnesium, in three different states (i.e., extruded, homogenized, and deformed by High-Pressure Torsion (HPT)), was investigated by immersion tests and electrochemical tests in a simulated physiological environment.

Immersion tests were carried out for 1, 2, and 3 weeks, and the corrosion rates of the studied materials were calculated using the weight loss method. Electrochemical tests, including open circuit potential (OCP) measurements and potentiodynamic polarization (PDP) scans, were also performed to assess the corrosion behavior.

The immersion test results indicated that the HPT-deformed samples showed a higher corrosion rate (0.24 mm/year) after one week of immersion due to the high grain boundary density formed by the HPT process. After three weeks, similar corrosion rates were observed in all samples (0.22 – 0.24 mm/year).

In the electrochemical tests, the measured OCPs showed relatively lower values for both HPT -deformed samples, indicating higher corrosion rates than the other samples. The information on the initial corrosion behavior of the investigated materials was provided by PDP scans where the measured curves were similar for all samples. The calculated electrochemical corrosion rates showed that the samples out of Zn-1Mg have relatively higher corrosion rates than those out of Zn-0.5Mg, however, the electrochemical tests have a high variability which makes the results less reliable.

Kurzfassung

Viele Forscher interessieren sich zunehmend für biologisch abbaubare metallische Materialien wie Eisen, Magnesium und Zink, indem diese die nachteiligen Wirkungen dauerhafter Materialien für orthopädische Implantate und Gefäß-Stents vermeiden. Kürzlich wurden insbesondere Materialien aus Zink bzw. Zink-Legierungen aufgrund ihrer angemessenen Bioabbaubarkeitsrate, die zwischen denen von Eisen und Magnesium liegt, als vielversprechendere Kandidaten vorgeschlagen.

In dieser Studie wurde das Korrosionsverhalten von zwei binären Legierungen auf Zinkbasis mit 0.5 und 1 Gewichtsprozent Magnesium in drei verschiedenen Zuständen (d. h. extrudiert, homogenisiert und mittels Hochdrucktorsion (HPT-) verformt) untersucht, mittels Immersionstests und elektrochemische Tests in einer simulierten physiologischen Umgebung.

Tauchtests wurden für 1, 2 und 3 Wochen durchgeführt, und die Korrosionsraten der untersuchten Materialien wurden mittels der Gewichtsverlustmethode bestimmt. Zur Bewertung des Korrosionsverhaltens wurden auch elektrochemische Tests durchgeführt, darunter Messungen des Leerlaufpotentials (OCP) und Scans der potentiodynamischen Polarisation (PDP).

Die Ergebnisse der Tauchtests zeigten, dass die HPT-verformten Proben nach 1 Woche eine höhere Korrosionsrate (0.24 mm/Jahr) aufweisen, was mit der durch das HPT-Verfahren erhöhten Korngrenzendichte erklärt werden kann. Nach drei Wochen wurden bei allen Proben ähnliche Korrosionsraten beobachtet (0.22 – 0.24 mm/Jahr).

In den elektrochemischen Tests zeigten die gemessenen OCPs relativ niedrigere Werte für beide HPT-verformten Proben, was auf höhere Korrosionsraten als bei den anderen Proben hinweist. Informationen über das anfängliche Korrosionsverhalten der untersuchten Materialien konnten den PDP-Scans entnommen werden, bei denen die gemessenen Kurven für alle Proben ähnlich waren. Die berechneten elektrochemischen Korrosionsraten zeigten, dass die Zn-1Mg Proben relativ höhere Korrosionsraten aufweisen als die Zn-0.5Mg Proben; die elektrochemischen Tests weisen jedoch eine hohe Variabilität auf, was die Ergebnisse weniger zuverlässig macht.

Abbreviations

A	Exposed sample surface area	[cm^2]
AIT	Austria Institute of Technology	
ARB	Accumulative roll bonding	
ASTM	American Society for Testing and Materials	
Ca	Calcium	
CE	Counter electrode	
Cl	Chlorine	
Co	Cobalt	
CR_E	Corrosion rate by electrochemical test	[mm $year^{-1}$]
CR_W	Corrosion rate by weight loss method	[mm $year^{-1}$]
c-SBF	Corrected simulated body fluid	
Cu	Copper	
d	Density	[g cm^{-3}]
DMEM	Dulbecco's modified Eagle medium	
E	Potential	[V vs reference]
E.W.	Equivalent weight	[g $equivalent^{-1}$]
EBSS	Earle's balanced salt solution	
ECAP	Equal channel angular pressing	
E_{corr}	Corrosion potential	[V vs reference]
E_{crev}	Crevice potential	
EIS	Electrochemical impedance spectroscopy	
EMD	Electrical discharge machine	
E_{pit}	Pitting potential	[V vs reference]
E_{tr}	Transpassive potential	[V vs reference]
F	Faraday's constant (= 96485)	[C $mole^{-1}$]
FBS	Fetal bovine serum	
Fe	Iron	
HBSS	Hank's balanced salt solution	
HE	Hydrostatic extrusion	
HEPES	4-(2-hydroxyethyl)-1-piperazineethanesulfonic acid	
HPT	High-Pressure Torsion	
HV	Vickers pyramid number	
i	Current	[A]
I	Current density (= i/exposed sample surface area)	[A cm^{-2}]
I_{corr}	Corrosion current density	[A cm^{-2}]

I_{net}	Net current density	[A cm^{-2}]
m	Number of moles in a corroded mass M	
M	Corroded mass	[g]
Mg	Magnesium	
$Mg(OH)_2$	Magnesium hydroxide	
MgO	Magnesium oxide	
n	Number of electrons required in the half-cell reaction	
Ni	Nickel	
n-SBF	Newly improved simulated body fluid	
OCP	Open circuit potential	
P	Phosphorus	
PBS	Phosphate-buffered saline	
PDP	Potentiodynamic polarization	
Q	Charge	[C]
RE	Reference electrode	
r-SBF	Revised simulated body fluid	
S	Sulfur	
SBF	Simulated body fluid	
SHE	Standard hydrogen electrode	
SPD	Severe plastic deformation	
Sr	Strontium	
t	Immersion time	[h]
TRIS	Trisaminomethane or THAM	
W	Atomic weight	
WE	Working electrode	
w_f	Final weight after corrosion products removal	[g]
w_i	Initial weight before immersion	[g]
WL	Weight loss per unit area	[g cm^{-2}]
Zn	Zinc	
$Zn(OH)_2$	Zinc hydroxide	
ZnO	Zinc oxide	
β_a	Anodic Tafel slope	[V $decade^{-1}$]
β_c	Cathodic Tafel slope	[V $decade^{-1}$]
ε	Strain	
σ_{UTS}	Ultimate tensile strength	[MPa], [GPa]

Table of contents

Chapter 1

Introduction

1.1 Background on biodegradable metallic materials

Non-degradable metallic materials, such as austenitic stainless steel, cobalt-chromium alloys, and titanium alloys, have been commercially employed in orthopedic implants (i.e., plates, pins, and screws) and cardiovascular interventional devices due to their good mechanical properties, biocompatibility, and high corrosion resistance [1], [2], [3].

However, the implant for a bone fracture treatment is no longer required after the healing of the fracture. Furthermore, the presence of long-term metallic implants may result in the release of toxic ions into the human body, and it can cause harmful diseases such as allergy, inflammation, neuropathy, Alzheimer's, and can have carcinogenic effects [4]. Therefore, most of the applications should be removed through secondary surgery when the recovery process is completed [3].

For these reasons, biodegradable metallic elements such as iron (Fe), magnesium (Mg), zinc (Zn), and their alloys have received significant attention as promising alternatives to permanent implants over the past several decades [3]. Especially, the research on biodegradable metal implants for medical applications has primarily focused on iron, magnesium, and their related alloys.

1.1.1 Iron

Iron is one of the most abundant metal ions in the human body, 3 - 5 grams of iron exist in the blood [5]. As biodegradable implant materials, iron and iron-based alloys have excellent biocompatibility and mechanical properties [6]. However, according to the results of animal

testing using an iron tube stent by Peuster *et al*. (2006) [7], it was observed that a large portion of the stent remained in the blood vessel after 12 months of implantation due to the very slow degradation process of iron in the physiological environment. This result indicates that similar problems as the permanent metallic applications may occur in the human body.

1.1.2 Magnesium

Magnesium is essential to human life and involved in many physiological functions, with the human body containing 25 – 35 grams of magnesium. Most of it presents in bones and muscles [5]. Magnesium and magnesium-based alloys have already been extensively investigated in clinical studies [8] and through *in vivo* tests by many researchers with successful results due to their good mechanical properties, biodegradability, and biocompatibility [9]. However, due to the high corrosion rate, magnesium implants can lead to the accumulation of hydrogen gas in bubbles, increase the pH value in the surrounding tissue, and lose their mechanical integrity during the degradation process [10].

1.1.3 Zinc

Due to the above-mentioned problems with iron and magnesium, zinc and zinc-based alloys have drawn attention as new candidates for biodegradable implants. Zinc is an essential element in the human body, which maintains approximately 2 – 4 grams of zinc in the prostate, eyes, brain, muscles, bones, kidneys, and liver [5]. Zinc plays a major role in the immune system and it is also regarded as an essential element for wound healing, synthesis of protein and DNA, and cell division [5].

One of the main advantages of zinc as a biodegradable implant material is its suitable corrosion rate. The standard corrosion potential of pure zinc is -0.763 V_{SHE}, which is between magnesium (-2.37 V_{SHE}) and iron (-0.44 V_{SHE}) [11], as shown in **Figure 1.1**.

Material	Reaction	Standard potential [V] at 25°C vs SHE
Nickel (Ni)	$Ni^{2+} + 2e^- \rightarrow Ni$	-0.250
Cobalt (Co)	$Co^{2+} + 2e^- \rightarrow Co$	-0.277
Iron (Fe)	$Fe^{2+} + 2e^- \rightarrow Fe$	-0.440
Chromium (Cr)	$Cr^{3+} + 3e^- \rightarrow Cr$	-0.74
	$Cr^{2+} + 2e^- \rightarrow Cr$	-0.91
Zinc (Zn)	$Zn^{2+} + 2e^- \rightarrow Zn$	-0.763
Manganese (Mn)	$Mn^{2+} + 2e^- \rightarrow Mn$	-1.18
Zirconium (Zr)	$Zr^{4+} + 4e^- \rightarrow Zr$	-1.53
Titanium (Ti)	$Ti^{2+} + 2e^- \rightarrow Ti$	-1.63
Aluminum (Al)	$Al^{3+} + 3e^- \rightarrow Al$	-1.66
Magnesium (Mg)	$Mg^{2+} + 2e^- \rightarrow Mg$	-2.37
Calcium (Ca)	$Ca^{2+} + 2e^- \rightarrow Ca$	-2.87
Lithium (Li)	$Li^{+} + e^- \rightarrow Li$	-3.05

Figure 1.1. Standard corrosion potential at 25 ℃. SHE is the standard hydrogen electrode. (Data based on reference [11])

This indicates that dissolution in the physiological medium of pure Zn is slower than magnesium and faster than iron, which can compensate for the drawbacks of magnesium and iron, as mentioned above. The recommended daily allowance for zinc is 11 mg for women, 8 mg for men, and 11 - 12 mg for pregnant and lactating women, but exposure to an excessive amount of zinc may cause toxicity and adverse effects on the human body [12]. However, Bowen *et al.* (2015) [13] showed with *in vivo* experiments, that there was no cell hyperplasia or chronic inflammation in cells surrounding implanted pure zinc wire into the abdominal aorta of the rat over 6.5 months. Following this, Yang *et al.* (2017) [14] implanted pure zinc stents into the rabbit abdominal aorta for 12 months. The mechanical integrity of pure zinc stents was maintained after 6 months. It was confirmed that 42 ± 30 % of the volume corroded after 12 months without serious inflammation, platelet aggregation, formation of thrombosis or intimal hyperplasia.

Nonetheless, due to the poor mechanical properties (σ_{UTS} ~ 30 MPa, $\varepsilon < 0.25$ %) of pure zinc,

it is unsuitable for use in most medical applications. Researchers aim to improve the mechanical properties of pure zinc by the thermodynamical refinement of grain size, extrusion, rolling, and alloying [3]. Li *et al*. (2015) [15] reported successful improvements in mechanical properties, corrosion behavior, and *in vitro* and *in vivo* biological compatibility of the cast, rolled, and extruded zinc binary alloys: Zn-1Mg, Zn-1Ca, and Zn-1Sr. The ultimate tensile strength (UTS) and elongation of as-extruded Zn-1Mg improved up to σ_{UTS} ~ 270 MPa and ε ~ 7 %, approximately. Mostaed *et al*. (2016) [16] compared mechanical and corrosion properties of pure zinc and 6 different Zn-based alloys after hot extrusion, and recommended that Zn-0.5Mg is the most promising candidate for biodegradable stent applications due to the suitable strength, ductility, strain hardening exponent and an appropriate rate of loss of mechanical integrity during corrosion (see **Figure 1.2**).

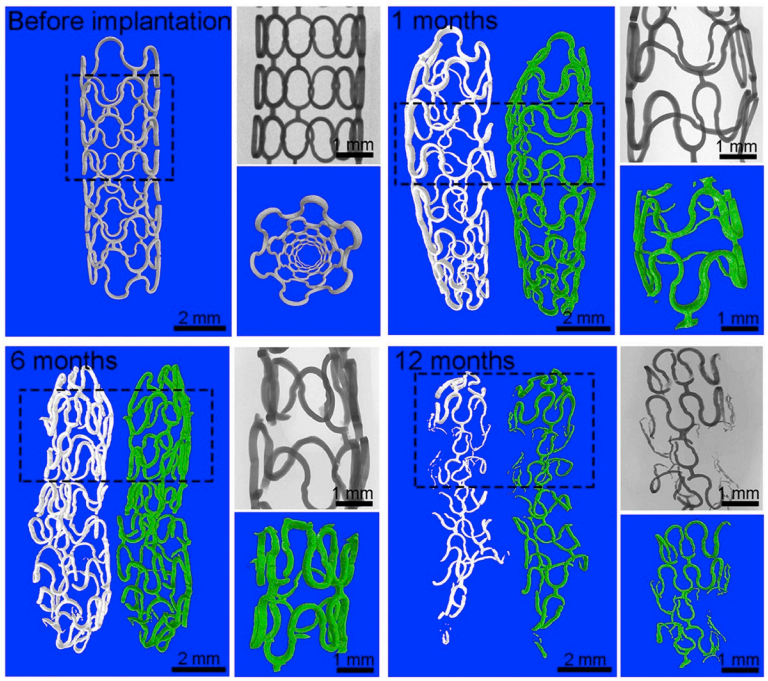

Figure 1.2. The micro-CT images of pure zinc stents in the aorta of rabbits after 0, 1, 6, and 12 months of implantation [14].

1.2. Ideal applications for biodegradable metallic materials

Biodegradable materials have been widely researched and are considered ideal biomedical materials. The following devices are the most frequently proposed medical applications for biodegradable metallic materials.

1.2.1 Biodegradable vascular stent

A biodegradable vascular stent is designed to keep blocked arteries open during the rebuilding process, and gradually corrode over time without harm to the human body, and then be completely dissolved within 12 to 24 months after completion of the healing period as shown in **Figure 1.3(a)** [17], [18].

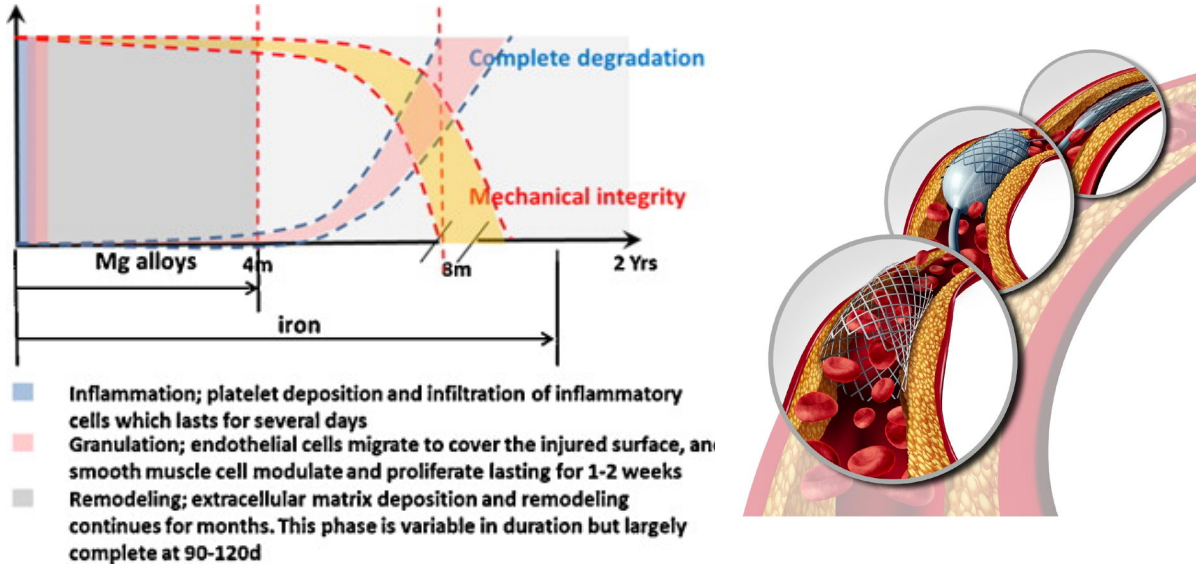

(a) (b)

Figure 1.3. (a) compromise between mechanical integrity and degradation of a biodegradable stent as a function of time [17] and (b) Illustration of the procedure of stent placement in a blood vessel [18].

The placement of a compressed stent is performed using a balloon-tipped catheter, and located in an occluded or narrowed artery, where the balloon is inflated to expand the mounted stent. Afterward, the balloon is deflated, and the catheter removed leaving the implanted stent to keep the narrowed artery open for restoration of blood flow. **Figure 1.3(b)** shows an illustration of the procedure of stent placement in a blood vessel [17].

The biodegradable stents should consist of a non-toxic element, and they should be maintaining their full mechanical integrity for a period of 4 to 6 months during the rebuilding process. The strength of the stent must be strong enough to maintain the dilatation of the narrowed blood vessel. The critical Young's modulus of stent material is not clearly defined, however, a high value is preferred to avoid recoil of the stent, which causes the acute vessel closure [20].

The required mechanical properties, biocompatibility, and corrosion rate of metallic biodegradable stents are summarized in **Table 1.1**, based on the research by Mostaed *et al*. (2018) [18], Bowen *et al*. (2013) [19], and Bowen *et al*. (2016) [20].

Table 1.1. Desired properties of biodegradable materials for vascular stents. (Data based on references [18], [19], [20])

Characteristics	Requirements
Biocompatibility	Non-toxic element, not causing inflammation and hypoallergenic reaction
Mechanical properties	
Ultimate tensile strength (UTS)	> 300 MPa
Elongation	> 15 – 18 %
Mechanical integrity maintenance period	4 - 6 months (12 - 24 months for full degradation)
Elastic recoil on expansion	< 4 %
Corrosion rate	< 0.02 mm/year

Many studies on biodegradable stents using magnesium-based alloy are still being conducted by many researchers and companies. The first clinical trial using a drug-eluting magnesium-

based absorbable metal scaffold (DREAMS by Biotronik, Bülach, Switzerland) for 6 months was published in 2013 by Haude *et al*. (2013) [21], and the results indicated that the stents had good biocompatibility without causing cardiac death and scaffold thrombosis.

1.2.2 Biodegradable orthopedic implants for bone fractures

As mentioned in the previous chapter, concerning the disadvantages of permanent implants for bone fracture treatment, biodegradable implants have gained the attention of many researchers as a substitute for traditional implants.

The properties of biodegradable implants (e.g., plates, screws, and pins) used to treat bone fractures are very similar to those of biodegradable stents. The necessary material properties of biodegradable orthopedic implants are summarized in **Table 1.2**.

Table 1.2. Desired properties of biodegradable materials for orthopedic implants. (Data based on the reference [22])

Characteristics	Requirements
Biocompatibility	Non-toxic element, not causing inflammation and hypoallergenic reaction
Mechanical properties	
Ultimate tensile strength (UTS)	> 300 MPa
Elongation	> 15 – 18 %
Mechanical integrity maintenance period	3 - 6 months (12 - 24 months for full degradation)
Elastic modulus	10 - 20 GPa (similar to cortical bone) desirable
Corrosion rate	< 0.5 mm/year, for plates and screws

The device must retain sufficient mechanical support during the fracture healing time (see **Figure 1.4(a)**), and the duration varies depending on the type of bone [17].

The compression screw MAGNEZIX® (Syntellix AG, Hanover, Germany), as shown below

in **Figure 1.4(b)**, was the first magnesium implant certified for human use. The device consists of magnesium-based alloy MgYREZr, which consists of more than 90 wt % of magnesium with alloying elements: yttrium, rare earth metal, and zirconium [25]. It has shown successful results in various animal testing and also clinical trials [23], [24], [25], [26].

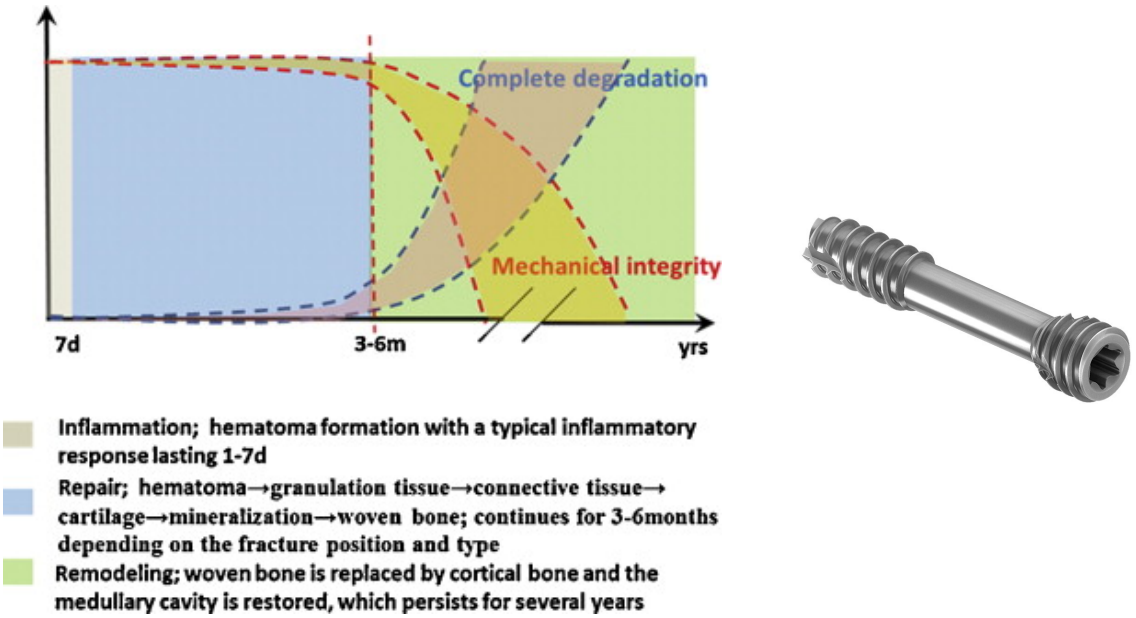

(a) (b)

Figure 1.4. (a) compromise between mechanical integrity and degradation of a biodegradable implant as a function of time [17] and (b) MAGNEZIX® SC produced by Syntellix AG, Hanover, Germany [26].

1.3 Aim of this work

The main goal of this study was to evaluate the corrosion behavior and rate of six different zinc-based materials. Zinc alloys with 0.5 and 1 weight percent of magnesium in three different conditions were investigated: extruded, homogenized, and processed by High-Pressure Torsion (HPT). The names of examined samples are as follows: Zn-0.5Mg, Zn-0.5Mg^{hom}, Zn-0.5Mg^{HPT}, Zn-1Mg, Zn-1Mg^{hom}, and Zn-1Mg^{HPT}.

Homogenization and HPT treatments were performed to enhance the mechanical properties of the samples. Homogenization was done at 180 ℃ for 96 hours. Additionally, the HPT process was performed at a pressure of 6 GPa for 1 turn at 0.2 rpm at room temperature.

All the degradation experiments were done at the AIT Austrian Institute of Technology, Center for Health & Bioresources, in a physiological environment close to the human body (simulated body fluid at 37 ± 1 ℃ with an initial pH value of 7.4).

Immersion tests and electrochemical tests were conducted; The immersion tests were performed for 1, 2, and 3 weeks. After the different periods of exposure, the corrosion rate was determined by the weight loss method after corrosion product removal. In the electrochemical tests, open circuit potential (OCP) and potentiodynamic polarization (PDP) methods were employed to observe the corrosion behavior.

Additionally, observations of the sample surface were made through light microscopy and visual inspection.

Chapter 2

State of the art

2.1 Biodegradation mechanism

2.1.1 Basic principles of corrosion

Corrosion of metals in an aqueous solution is a type of coupled electrochemical reaction, which is known as the 'half-cell reaction'. It is divided into anodic half- and cathodic half-reactions by losing and gaining electrons between the anodic and the cathodic site, as presented in **Figure 2.1**. The equations in this Figure were written according to the literature [17].

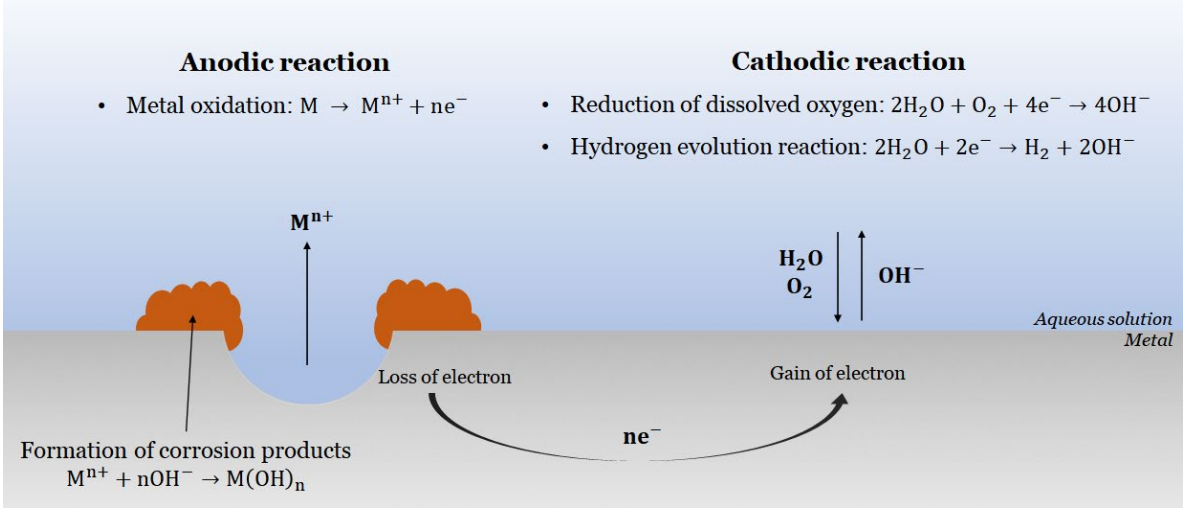

Figure 2.1. Corrosion process of metal in an aqueous solution.

In an anodic reaction, the oxidation of the metal occurs, which releases metal ions (M^{n+}) into the solution. As a result of this process, electrons decrease at the anodic site. In a cathodic

reaction, the reduction of dissolved oxygen and the hydrogen evolution reaction (i.e., the reduction of water) occurs by gaining electrons from the anodic site [27].

2.1.2 Corrosion behavior of pure zinc in the simulated body fluid

The degradation stages of pure zinc in the revised simulated body fluid (r-SBF) solution are shown in **Figure 2.2**. (For further discussion of the simulated body fluid, see **Chapter 3.2**)

The metallic state of zinc oxidizes to the ionic state Zn^{2+} (**Equation (2.1)**), and in this process, zinc at the anodic site loses electrons. These electrons are consumed for the reduction reaction of dissolved oxygen which is the main reaction at the cathodic site. (**Equation (2.2)**)

Unlike the corrosion behavior of magnesium, the corrosion products of zinc (i.e., $Zn(OH)_2$ and ZnO) tend to accumulate on the sample surface as described in **Equation (2.3)** and **Equation (2.4)**, as shown in **Figure 2.2**, without H_2 gas evolution [17], [28].

$$Zn \rightarrow Zn^{2+} + e^{-} \tag{2.1}$$

$$O_2 + H_2O + 4e^{-} \rightarrow 4OH^{-} \tag{2.2}$$

$$Zn^{2+} + 4OH^{-} \rightarrow Zn(OH)_2 \tag{2.3}$$

$$Zn(OH)_2 \rightarrow ZnO + H_2O \tag{2.4}$$

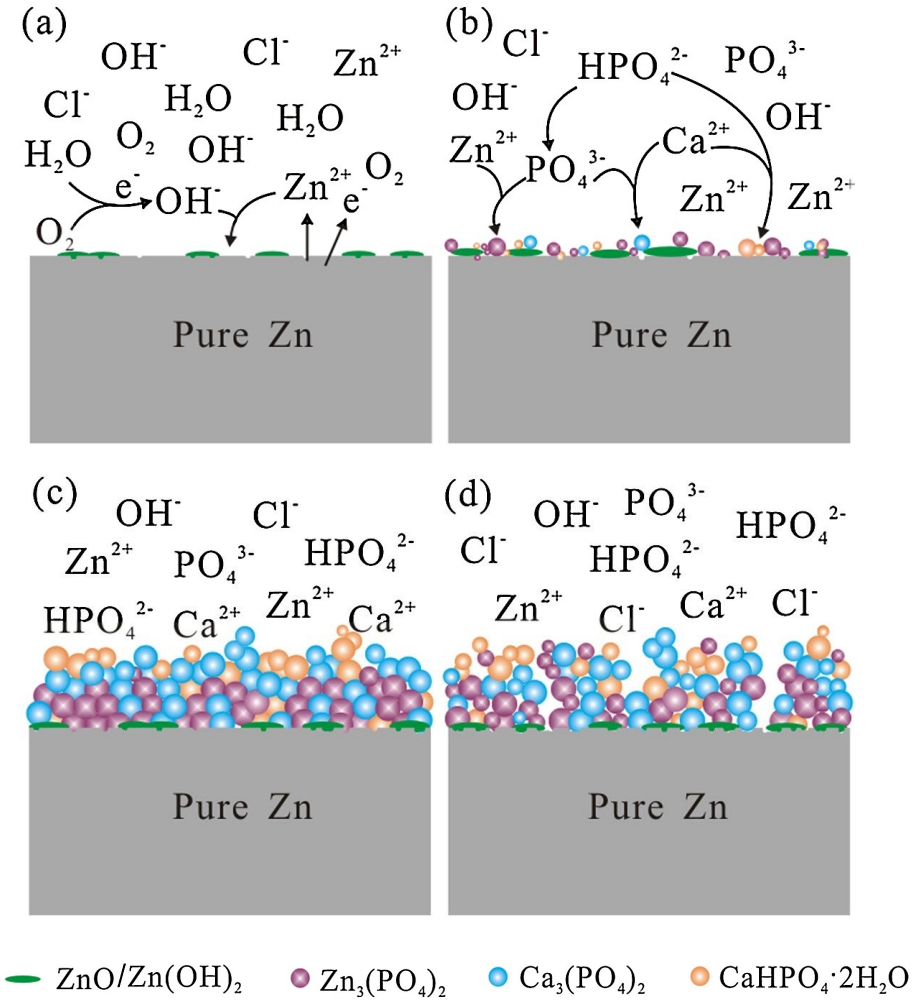

Figure 2.2. Schematic illustration of corrosion process of pure zinc exposed to the r-SBF solution (a) zinc is dissolved and $Zn(OH)_2$ and ZnO are formed the at the initial stage of immersion, (b) formation of $Zn_3(PO_4)_2$, $Ca_3(PO_4)_2$, and $CaHPO_4 \cdot 2H_2O$ with increasing immersion time, (c) growth and thickening of corrosion products layer, and (d) the corrosion products are partially dissolved [28].

This tendency can be also explained by the Pourbaix diagram [74]. The pH value of the r-SBF solution increases due to the release of the OH^- ions, resulting in the formation of $Zn(OH)_2$, as shown in **Figure 2.3**.

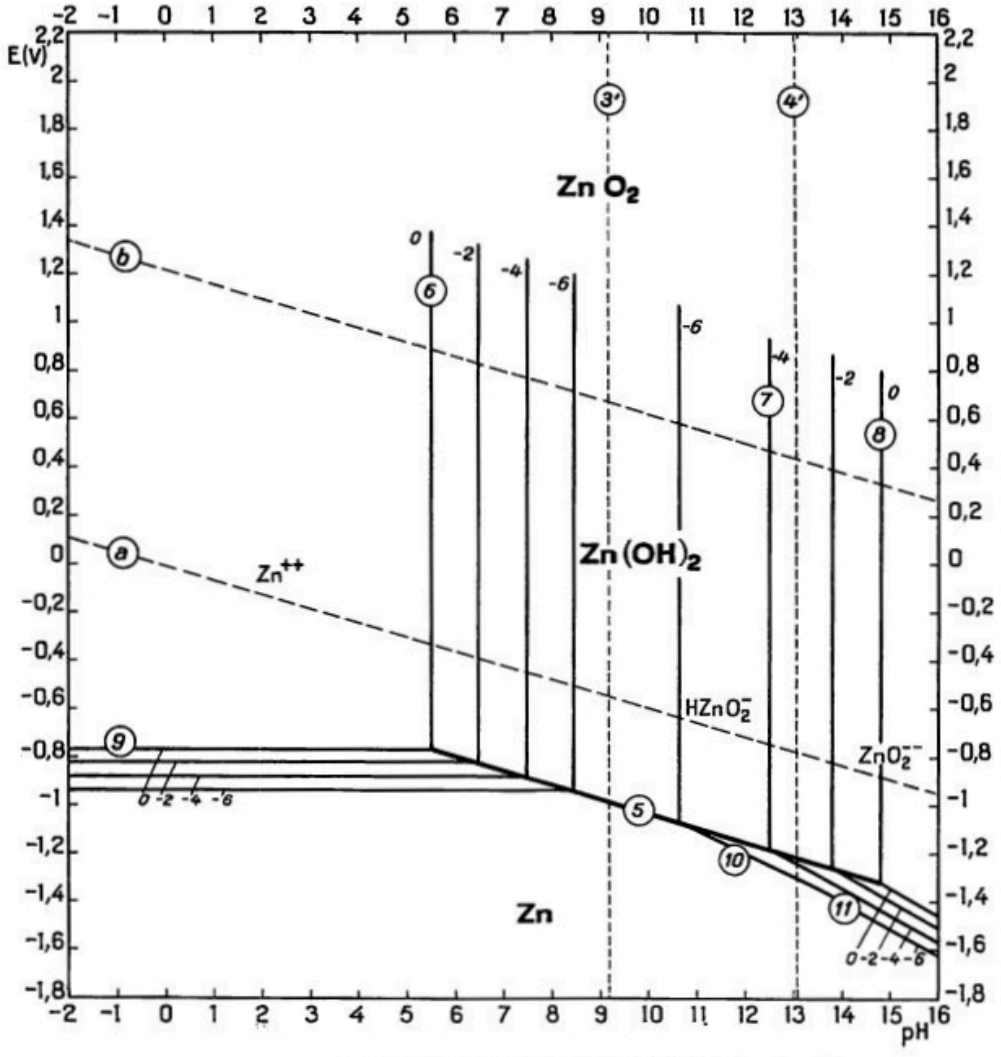

Figure 2.3. Pourbaix diagram for the system zinc-water at 25 °C [74]**.**

When the immersion time increases, the zinc oxide film is gradually destroyed by aggressive ions, such as Cl^- and SO_4^{2-}. The equations are as follows [30]:

$$Zn(OH)_2 + 2Cl \rightarrow ZnCl_2 + 2OH^- \quad (2.5)$$

$$Zn(OH)_2 + SO_4^{2-} \rightarrow ZnSO_4 + 2OH^- \quad (2.6)$$

Meanwhile, the phosphates molecules, such as $Zn_3(PO_4)_2$ and $Ca_3(PO_4)_2$, start to form on the surface due to the formation of zinc oxide. Simultaneously, nucleation of $CaHPO_4 \cdot 2H_2O$ occurs as result of the interaction between HPO_4^{2-} and Ca^{2+}, according to the following **Equation (2.7)** to **Equation (2.10)**.

$$HPO_4^{2-} + OH^- \rightarrow PO_4^{3-} + H_2O \quad (2.7)$$

$$3Zn^{2+} + 2PO_4^{3-} \rightarrow Zn_3(PO_4)_2 \quad (2.8)$$

$$3Ca^{2+} + 2PO_4^{3-} \rightarrow Ca_3(PO_4)_2 \quad (2.9)$$

$$Ca^{2+} + HPO_4^{2-} + 2H_2O \rightarrow CaHPO_4 \cdot 2H_2O \quad (2.10)$$

The size of phosphates particles increases and forms a corrosion product layer with increasing time, which protects the surface of the sample from the solution as shown in **Figure 2.2(c)**. A thick corrosion product layer lowers the corrosion rate, which means less zinc ions are dissolving from the sample into the solution, as a result, the OH^- ions are decreased [28].

As corrosion products accumulate on the sample surface with increasing immersion time, partial dissolution of corrosion products (cracks) may occur (see **Figure 2.2(d)**) due to stresses in the corrosion product layer, and it can no longer protect the sample efficiently [28].

2.2 Influence factors on the corrosion behavior

2.2.1 Trace impurity elements

Trace impurity elements that are introduced during the material manufacturing process affect the corrosion rate. It has been proven in some early studies; McNulty *et al*. (1943) [29] investigated the corrosion behavior of high purity magnesium and magnesium-based alloys by electrochemical test and hydrogen evaluation method. They concluded that the presence of different trace impurity elements in the metal affects the corrosion behavior. Hanawalt *et al*. (1942) [31] studied the influence of impurities on the corrosion rate of magnesium-based binary alloys. They reported that the corrosion rate of alloys significantly increases when the material contains impurities, such as copper (Cu), iron (Fe), nickel (Ni), and cobalt (Co), above their respective tolerance limits, as shown in **Figure 2.4.**

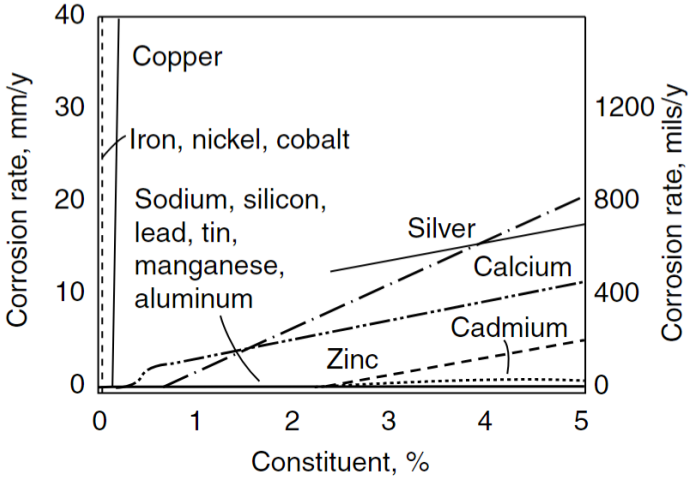

Figure 2.4. Influence of trace impurity elements on the corrosion rate of magnesium-based alloys immersed in 3% NaCl solution [31]. Reproduced by [32].

Therefore, the presence of trace impurity elements needs to be controlled carefully during the manufacturing process to achieve desired corrosion rate, and the chemical composition of impurity elements should be included for detailed discussion.

2.2.2 Grain size refinement and presence of secondary phase

As discussed in the previous chapter, the mechanical properties of pure zinc are poor for biodegradable applications, therefore, improving and enhancing their mechanical properties by the thermomechanical refinement of grain size, extrusion, rolling, and alloying is crucial. The various treatment conditions lead to changes in grain size and introduce a different amount of second phases into the metal.

In general, substantial grain refinement can be achieved by severe plastic deformation (SPD), which includes techniques like accumulative roll bonding (ARB), hydrostatic extrusion (HE), equal channel angular pressing (ECAP), and high-pressure torsion (HPT). Among those methods, HPT is a relatively simple and effective process to obtain extremely high shear strains even into brittle metals [83].

According to Hernández-Escobar, D. *et al.* (2019) [79], the corrosion rate of Zn-Mg hybrids (Zn/Mg/Zn disk) by HPT accelerated by intermetallic phases such as Mg_2Zn_{11} and $MgZn_2$, because they may as act a galvanic couple.

The grain size decreases with increasing weight percent of magnesium, and according to Mostaed *et al*. (2016) [16], the corrosion current density decreases with decreasing grain size, and it can be also seen that the corrosion rate of extruded zinc alloys, which have fine grain size, is slightly lower than that of coarse-grained as-casted alloys.

In the case of Zn-Mg alloys, according to the phase diagram (see **Figure 2.5**) of the system, magnesium has low solid solubility in zinc. When the liquid state (L) of Zn-Mg metal is cooled below 364 ℃, the intermetallic phase Mg_2Zn_{11} is formed at the grain boundary of primary zinc which formed previously [16], [33], [34]. It is investigated that this secondary phase Mg_2Zn_{11} shows a significant low corrosion rate not only in 3 % of NaCl solution [35] but also in atmospheric conditions [36].

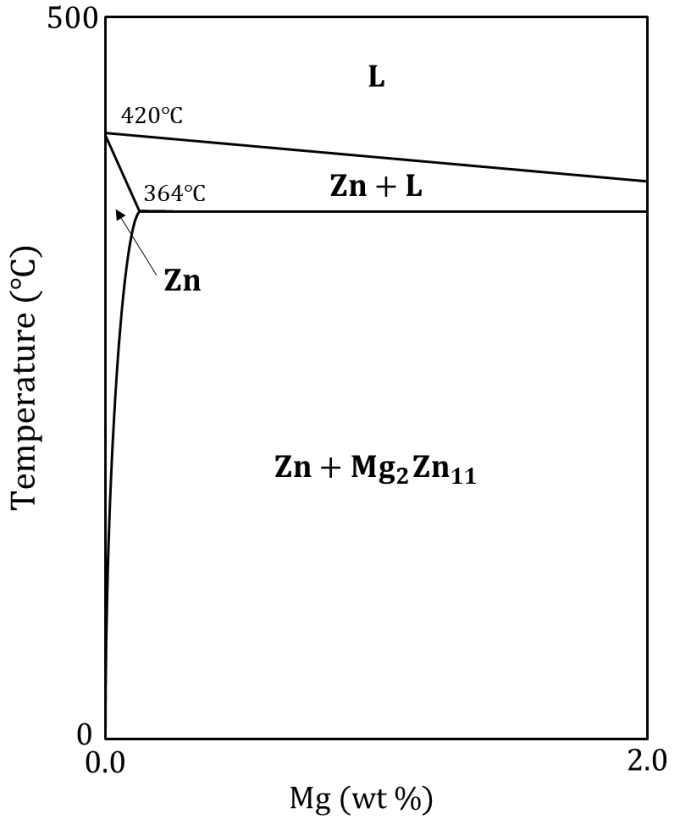

Figure 2.5. Phase diagram of zinc-magnesium. (Based on the literature [37])

2.2.3 Influence of measurement conditions

2.2.3.1 pH value

As mentioned in **Chapter 2.1.2.**, zinc ions released during the corrosion process promote the formation of $Zn(OH)_2$, resulting in an increased pH value.

Tomas *et al*. (2012) [38] investigated the corrosion behavior of zinc in 0.1 mole NaCl solution as a function of pH value in the range of 1 to 13 using electrochemical measurement. They concluded that the overall corrosion rate is decreased due to the lowered cathodic reaction rate in the pH range of 7 to 10.

Meng *et al.* (2019) [39] observed a change in the pH value of the saline solution (0.9 % NaCl) during pure zinc immersion for 2 weeks and showed that the pH value gradually increased with time. This increase in pH gradually slowed down after 48 hours due to the reaction of part of $Zn(OH)_2$ with OH^- to form $Zn(OH)_4^{2-}$. A similar slow increase of pH value is also observed in the r-SBF solution by Liu *et al.* (2018) [28] as shown in **Figure 2.6**.

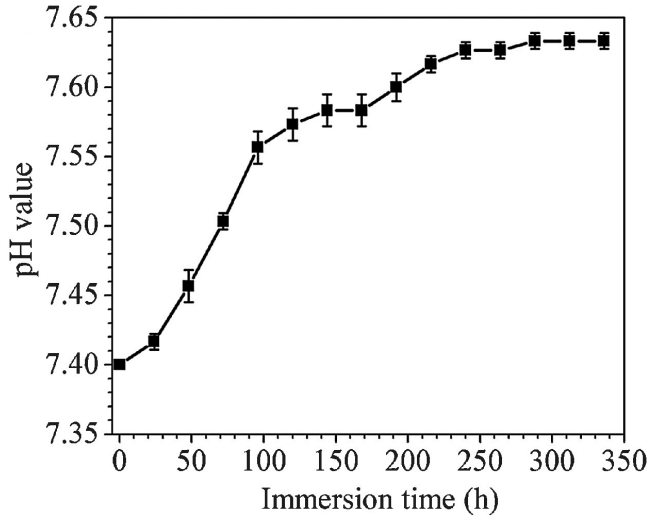

Figure 2.6. change in the pH as a function of immersion time in r-SBF solution [28].

2.2.3.2 Temperature

Temperature can affect the accuracy of the experiment, Feliu *et al*. (2019) [40] found an increased corrosion rate of the magnesium-based alloy (AZ31B) with increasing temperature in Ringer's solution, and it was also confirmed that the corrosion rate after 4 days of immersion at 37 ℃ was approximately 4 times higher than the corrosion rate at 20 ℃. The average size of pits also increased with increasing temperature, from 105 µm to 407 µm in depth and from 256 µm to 1857 µm in width. In the case of zinc, rapid corrosion at higher temperatures was also demonstrated; the corrosion rates of zinc in distilled water were approximately 1.9 and 3.3

times higher at 45 ℃ and 65 ℃ than at room temperature, respectively [41]. In general, the influence of temperature on *in vivo* and *in vitro* biodegradation is still not clearly defined and understood, due to the lack of research.

2.2.3.3 Electrolyte system

One of the most important factors influencing corrosion behavior is the electrolyte. There are various electrolyte systems employed in *in vitro* experiments: saline solution (0.9 % NaCl), Hank's solution, various types of simulated body fluid (SBF) solution, phosphate-buffered solution (PBS), and Dulbecco's modified Eagle medium (DMEM).

Many researchers have published the results of the *in vitro* tests using simple solutions like a saline solution to understand the basics of corrosion behavior of selected material. However, simple solutions do not contain complex ions which cause various reactions in the human body. Therefore, it is not suitable to describe the biodegradation process in a physiological environment using simple solutions.

As discussed in **Chapter 2.1.2**, when the metallic zinc is immersed in a solution that contains chloride (Cl^-) and sulfate (SO_4^{2-}) ions, they will form $ZnCl_2$ and $ZnSO_4$ with zinc metal ions which can dissolve the oxide protective film such as ZnO and $Zn(OH)_2$ [30].

In *in vitro* experiments, the pH value of the electrolyte is adjusted using a buffer solution such as Tris, HEPES, or $NaHCO_3/CO_2$. Liu *et al*. (2019) [47] reported the effect of the different buffer systems in NaCl solution and SBF on the corrosion behavior of pure zinc. They found that Tris-HCl hinders the formation of corrosion products and increases the corrosion rate of pure zinc. HEPES and $NaHCO_3/CO_2$ accelerate the formation of passive films on the sample surface in NaCl solution and decrease the corrosion rate. In SBF, on the other hand, the addition of HEPES and $NaHCO_3/CO_2$ reduces the accumulation of corrosion product and promotes the corrosion process.

The presence of organic compounds can also influence the corrosion process of zinc. Liu *et al*. (2019) [48] compared the corrosion rate of pure zinc in 4 different solutions: Hank's solution,

SBF, DMEM, and DMEM+FBS (DMEM + 10 % fetal bovine serum). They found decreased zinc degradation by the formation of insolvable salts and organic components in DMEM, and the presence of protein promoted local corrosion and increased polarization resistance. Additionally, it was also concluded that the fastest corrosion occurred in SBF compared to other solutions. Törne *et al*. (2016) [49] discussed a similar influence of protein on pure zinc.

Dong *et al*. (2021) [50] compared the corrosion behavior of magnesium, zinc, and iron in SBF and DMEM, and discussed that the corrosion rate in DMEM is slower than in SBF because of the formation of a more protective layer, adsorbed amino acid, and absence of Tris-HCl.

The major ion concentration and buffer solution of electrolytes are summarized and compared to human blood plasma in **Table 2.1**.

Table 2.1. Ion concentrations of human blood plasma and various electrolytes.

Ion	Plasma [42]	Saline solution	EBSS (1) [44]	HBSS (2) [45]	Original SBF (3) [43]	PBS (4) [46]	DMEM (5) [46]
Na^+ ($mmol \cdot L^{-1}$)	142.0	153.0	143.5	142.1	142.0	157.0	127.3
K^+ ($mmol \cdot L^{-1}$)	5.0	-	5.4	5.3	5.0	4.1	5.3
Ca^{2+} ($mmol \cdot L^{-1}$)	2.5	-	1.8	1.26	2.5	-	1.8
Mg^{2+} ($mmol \cdot L^{-1}$)	1.5	-	0.8	0.9	1.5	-	0.8
HCO_3^- ($mmol \cdot L^{-1}$)	270.	-	26.2	4.2	4.2	-	44.1
Cl^- ($mmol \cdot L^{-1}$)	103.0	153.0	123.5	146.8	148.0	140.0	90.8
HPO_4^{2-} ($mmol \cdot L^{-1}$)	1.0	-	1.0	0.78	1.0	11.5	0.9
SO_4^{2-} ($mmol \cdot L^{-1}$)	1.0	-	0.8	0.41	0	-	0.8
Protein ($g \cdot L^{-1}$)	63-80	-	-	-	-	-	
Amino acid ($g \cdot L^{-1}$)	Variable	-	-	-	-	-	1.6
Glucose ($g \cdot L^{-1}$)	Variable	-	-	-	-	-	25
Buffer	-	-	-	-	TRIS	-	HEPES

(1) Earle's balanced salt solution, (2) Hank's balanced salt solution, (3) Simulated body fluid, (4) Phosphate-buffered saline, and (5) Dulbecco's Modified Eagle Medium

2.3 *In vivo* and *in vitro* method

The method for investigating the corrosion behavior of biodegradable materials is *in vivo* testing using an animal model which is closest to situation in the human body. Nonetheless, there are limitations of *in vivo* testing, such as ethics, cost, and time. Therefore, it is important to determine the suitability of a substance through appropriate pre-*in vitro* testing [51].

2.3.1 *In vivo*

The corrosion rate of *in vivo* test can be calculated in the following ways: the weight loss, the corrosion penetration rate using the reduction of the cross-sectional area [55], and the volume loss measured by micro-CT [15].

The *in vivo* corrosion properties of pure zinc and zinc-based materials (e.g., wire, pin, rod, disk, stent, and strips) using animal models have been performed by several researchers [13], [14], [15], [52], [53], [54]. Bowen *et al*. (2013) [52] estimated the corrosion rate of pure zinc wire in a Sprague-Dawley rat artery over 6 months. The cross-sectional area of the wire decreased gradually with implantation time and the wire was maintained intact for up to 4 months. Zhou *et al*. (2019) [53] performed long-term *in vivo* implantation of a Zn-0.8Cu stent for up to 24 months in a porcine coronary artery, in which the stent preserved structural integrity after 6 months and showed appropriate corrosion rate without accumulation of corrosion products and inflammatory responses. Recently, Yang *et al*. (2020) [54] investigated the mechanical properties, biodegradability, and biocompatibility of pure zinc and zinc-based binary and ternary alloys through *in vivo* and *in vitro* experiments. In the *in vivo* test, at 8 weeks after implantation in the femurs of the rats, there was no significant degradation and a steady corrosion rate with the formation of new bone around the implant was shown.

2.3.2 *In vitro*

According to Kirkland *et al.* (2012) [51], there are two types of *in vitro* measurement: unpolarized and polarized methods.

2.3.2.1 Unpolarized methods

The unpolarized methods include: weight loss and hydrogen evaluation measurement, both are commonly used for studying *in vitro* degradation. In general, during the experiment, the temperature of the bottle containing the selected electrolyte and sample is maintained similar to the human body (approximately 37 ℃) through a water bath. However, the results may vary depending on the experimental set-up, such as selection of electrolyte, replacement of solution, temperature, pH value, addition of CO_2 gas into the electrolyte, and immersion period.

- **Weight loss measurement**

  The mass loss measurement is considered to be the easiest and simplest method for determining the general corrosion rate during the test period. The corrosion rate is simply calculated by the mass loss divided by the immersion time and the surface area. To achieve reliable results, the samples have to be cleaned properly before measuring the mass. According to the ASTM G1-03 [56], the corrosion product formed during the immersion test can be removed by the following procedure; first, remove it mechanically using a brush, then expose the sample to an appropriate chemical solution to remove corrosion products on the sample surface. Ultrasonic treatment is also recommended to remove tightly bounded corrosion products. The cleaning procedure of the specimen should be repeated, and the mass should be recorded and graphed to determine the final weight of the sample to calculate the corrosion rate.

- **Hydrogen evaluation measurement**

  The hydrogen evaluation measurement can be performed to determine the corrosion rate for samples, such as magnesium and magnesium-based alloys, that generate hydrogen gas during the corrosion process following the mechanism as described in **Equation (2.11)** [51].

$$Mg + 2H_2O = Mg^{2+} + 2(OH)^- + H_2 \quad (2.11)$$

2.3.2.2 Polarized methods

A polarized method, such as potentiodynamic polarization (PDP) and electrochemical impedance spectroscopy (EIS), is an experiment with the presence of an external 'driving force' [51] during the corrosion test using the electrochemical measurement system. The polarized method provides a significantly faster evaluation of corrosion properties compared with Unpolarized methods.

- **Electrochemical impedance spectroscopy (EIS)**

  Electrochemical impedance spectroscopy (EIS) is a commonly used electrochemical technique for analyzing corrosion properties. It measures the total impedance of the sample surface over a broad range of frequencies. Values for resistance and capacitance can be obtained using this method.

- **Potentiodynamic polarization (PDP)**

  Potentiodynamic polarization (PDP) is also widely employed electrochemical techniques using direct (DC) for assessing corrosion behaviors and corrosion characteristics. This method is discussed in the next following chapter in detail.

2.4 Electrochemical measurements

Electrochemical measurements are the most popular techniques to analyze the corrosion behavior of metallic material; The measurements are relatively rapid compared to the unpolarized method. It takes only a few minutes or hours depending on the setting. However, it should be noted that the electrochemical measurements are a type of accelerated corrosion experiment by the external driving force, therefore the results can be different from those of unpolarized methods [57]. The two electrochemical methods performed in this thesis are discussed in detail in the following chapter.

2.4.1 Open circuit potential

The open-circuit potential (OCP) measurement is a relatively easy and fast method, which gives the basic information about the corrosion state and corrosion behavior of the specimen surface [58]. It is also known as the zero-current potential or the rest potential which is the potential difference between the working electrode (WE; i.e., the sample) and the reference electrode (RE) without external current. In general, a positive shift in the OCP indicates decreasing surface activity, and a more negative OCP suggest increasing anodic dissolution [59], [60] (See **Figure 1.1** in **chapter 1**).

2.4.2 Potentiodynamic polarization scan

The potentiodynamic polarization (PDP) scan is one of the commonly used electrochemical techniques which can determine the kinetics of the corrosion process.

This technique measures the net current as a function of the working electrode (WE) potential while varying the potential at a fixed scan rate. Here, the net current means the sum of anodic and cathodic current, which passes through the electrochemical cell, because anodic current and cathodic current cannot be measured separately. The preferred current unit in the electrochemical method is current per unit area ($\mathrm{A\,cm^{-2}}$) because it depends on the working electrode surface [61].

In general, the direction of the potential scan starts from cathodic to anodic potential, which is called the 'anodic polarization scan' method, to prevent corrosion of the specimen at an anodic potential. A schematic of a typical anodic polarization curve for an active-passive material as a consequence of anodic and cathodic reactions is illustrated in **Figure 2.7**.

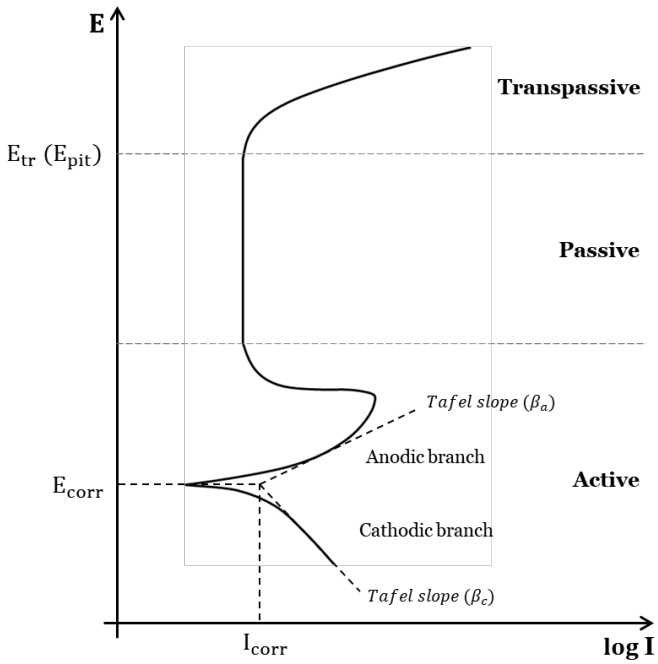

Figure 2.7. Schematic of the typical anodic polarization curve, where E is the potential and I is the current density.

In general, the potentiodynamic curve can be divided into three regions: active, passive, and transpassive region.

The scan often starts from a slight cathodic potential (below E_{corr}) and then electrochemical polarization appears on the cathodic and anodic branches. At higher potential, the current density rapidly increases during applied potential increases, and then, suddenly it drops due to the formation of a passive oxide layer on the sample surface. This layer protects the sample against corrosion.

As a result of the passive layer, the measured current density can maintain a relatively stable value over a wide range of potential when a steady state is reached, this region is called the passive region. In the transpassive region, the passive layer is damaged and pits form above the transpassive potential (E_{tr}) due to the high applied potential [62]. Depending on the type of corrosion, this potential can be called the pitting potential (E_{pit}) or the crevice potential (E_{crev}) [63].

Based on the work of Stern *et al*. (1957) [64] and Frankel (2002) [65], the mathematical description of the potentiodynamic polarization (PDP) scan can be written as follows:

$$I_{net} = I_{corr}\left[10^{\frac{E-E_{corr}}{\beta_\alpha}} - 10^{-\frac{E-E_{corr}}{|\beta_c|}}\right] \quad (2.12)$$

where I_{net} is the net current density, I_{corr} is the corrosion current density, E is the applied potential, and E_{corr} is the corrosion potential. β_α and β_c are the Tafel slopes from the anodic and cathodic half-cell reactions. At the corrosion potential E_{corr}, the cathodic and anodic reactions occur to the same amount. Therefore, the measured I_{net} is zero in an ideal case, as shown in **Figure 2.8**.

When the applied potential is sufficiently larger than the corrosion potential ($E \gg E_{corr}$), the second term of **Equation 2.12** is negligible, therefore the equation for the anodic branch is then given by:

$$E = E_{corr} + \beta_\alpha\left[\log(I_{net}) - \log(I_{corr})\right] \quad (2.13)$$

Similarly, the equation for the cathodic branch can be written as followed,

$$E = E_{corr} - \beta_c\left[\log(I_{net}) - \log(I_{corr})\right] \quad (2.14)$$

Figure 2.8 and **Figure 2.9** show schematic ideal plots of polarization around E_{corr}, which is known as the Tafel region, in linear and semi-logarithmic scales.

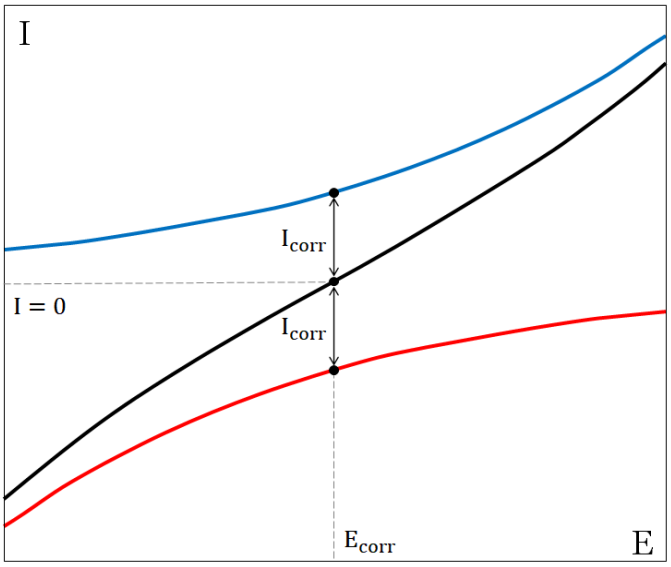

Figure 2.8. Schematic of a Tafel plot. Current density (I) as a function of potential (E). Cathodic current (blue line), anodic current (red line), and the measured net current (black line).

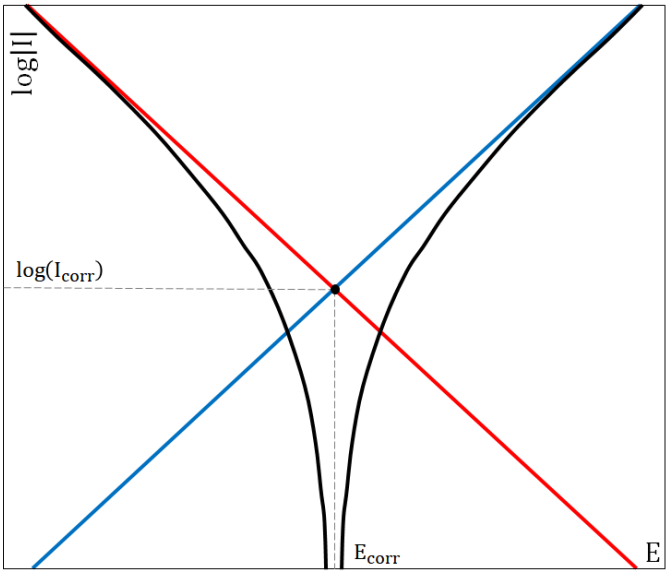

Figure 2.9. Schematic of a Tafel plot. Semi-logarithmic current density (log|I|) as a function of potential (E). Cathodic Tafel slope (blue line), anodic Tafel slope (red line), and the measured net current (black line).

2.4.3 Corrosion rate by electrochemical measurement

2.4.3.1 Equivalent weight

The definition of equivalent weight (E.W.) of pure elements is as follows

$$\mathrm{E.W.} = \frac{\mathrm{W}}{\mathrm{n}} \tag{2.15}$$

where W is the atomic weight of the element and n is the number of electrons required in the half-cell reaction.

For an alloy, E.W. can be calculated as [72]

$$\mathrm{E.W.} = \frac{1}{\sum \frac{\mathrm{n_i} \cdot \mathrm{f_i}}{\mathrm{W_i}}} \tag{2.16}$$

where W_i is the atomic weight of the i-th alloy element, n_i is the number of electrons required in the half-cell reaction of the i-th alloy element, and f_i is the mass fraction of the i-th alloy element

2.4.3.2 Corrosion rate from corrosion current

The equation of anodic-half cell reaction of metals can be defined as

$$\mathrm{Metal} \rightarrow \mathrm{Metal}^{n+} + \mathrm{ne}^{-} \tag{2.17}$$

where n is the number of electrons transferred in the half cell reaction.

The relation between the corrosion current and the mass transfer can be described based on Faraday's law. Assuming that the corroded mass is M gram during the reaction and there are m moles in M gram. The electrical charge Q can be described by the following **Equation (2.18).**

$$Q = n * F * m \tag{2.18}$$

Also known is

$$Q = \int i\,dt \tag{2.19}$$

where Q is the electrical charge in C, which is well known as time (t) integral over the current (i) as written as in **Equation (2.19)**, and F is the Faraday's constant (= 96485 C/mole).

The corroded mass M ($= m * \text{atomic mass (W)}$) can be defined with equivalent weight using **Equation (2.18)** and **Equation (2.15)**

$$Q = \frac{F * M}{E.W.} \tag{2.20}$$

using **Equation (2.19)**, time t can be simply written

$$t = \frac{F * M}{i * E.W.} \tag{2.21}$$

the unit of the corrosion rate is the length divided by the time.

Therefore, the general expression of corrosion rate with the corrosion current density and the conversion constant,

$$CR_E = \frac{I_{corr} * E.W.}{d * F} = C * \frac{I_{corr} * E.W.}{d} \quad (2.22)$$

where CR_E is the electrochemical corrosion rate, I_{corr} is the corrosion current density in A/cm^2, C is the conversion constant, and d is the density in g/cm^3. Here, it should be noted that the current (i) is substituted by the current density (I = i/exposed sample surface area).

Table 2.2 shows the conversion constants of the corrosion rate. In this calculation, E.W. is treated as a dimensionless quantity [72].

Table 2.2. Unit of corrosion rate, corrosion current, and corresponding conversion constant C [72].

CR_E unit	I_{corr} unit	d unit	C	C unit
mm/year	$\mu A/cm^2$	g/cm^3	$3.27 * 10^{-3}$	mm g/μA cm year

Chapter 3

Materials and methods

3.1 Materials investigated

In this study, two different zinc-based alloys (i.e., 0.5 and 1 wt % of magnesium) in 3 different states were investigated. The samples used in this work are summarized and listed in **Table 3.1**.

Table 3.1. List of the investigated specimens.

Sample	As-extruded	Homogenized	HPT
Zn-0.5Mg	○		
Zn-0.5Mg^{hom}	○	○	
Zn-0.5Mg^{HPT}	○	○	○
Zn-1Mg	○		
Zn-1Mg^{hom}	○	○	
Zn-1Mg^{HPT}	○	○	○

- **As-extruded (extrusion)**

  Pure zinc (99.995 wt % purity) and magnesium (99.9 wt % purity) alloys were weighted to the desired alloy compositions and melted in the induction furnace with a protective atmosphere consisting of sulfur hexafluoride (SF_6) gas. After melting and blending, the alloy was cast in an iron mold with a length of 120 mm and a diameter of 40 mm. After cooling, the alloys were heated up to 150 ℃ and finally extruded into a 10 mm diameter rod with an extrusion speed of 10 mm/sec. The extruded samples were provided by AGH University of Science and Technology in Kraków (Poland), Faculty of Non-Ferrous Metals.

- **Homogenization**

  The homogenized samples are prepared from the extruded rods in the following steps: cutting, grinding, and homogenization. The extruded rod-shaped sample was cut by an electrical discharge machine (EMD) into a disk shape and subsequently grounded with SiC paper of 400, 800, and 1200 μm grit to remove the surface layer damaged during the cutting process. Finally, the alloys were homogenized at 180 ℃ under a protective atmosphere of argon for 96 hours, followed by water quenching.

- **Severe plastic deformation (SPD)**

  Among the techniques for severe plastic deformation (SPD), the High-Pressure Torsion (HPT) process was performed to improve the sample's mechanical properties by refinement of grain size. The HPT process uses a disk-shaped thin sample and is applying high hydrostatic pressure and torsional strain through the upper and lower anvils [83] as illustrated in **Figure 3.1**. The homogenized samples were deformed by the HPT method at a pressure of 6 GPa for 1 turn at 0.2 rpm at room temperature.

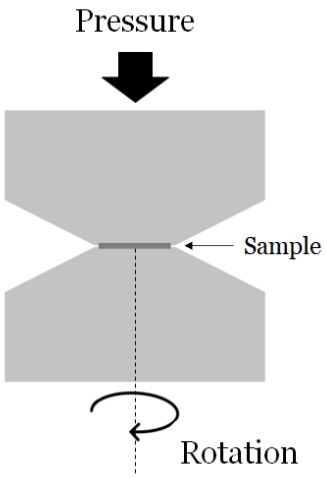

Figure 3.1 Schematic illustration of the High-Pressure Torsion (HPT) processing method. While applying pressure by the upper anvil, the lower anvil rotates.

These conditions were selected according to their higher hardness value compared to various other processing conditions. **Table 3.2** shows the microhardness values measured using a Vickers indenter. For the HPT-processed samples, the values given are the maximum hardness values achieved within the possible strain range. More information on the mechanical properties of the samples can be found in a master thesis of Lukas Aitzetmüller [84].

Table 3.2. Microhardness values of the investigated alloys in different conditions measured with a Vickers indenter in the unit of kgf/mm^2[84].

	Zn-0.5Mg [HV]	Zn-1Mg [HV]
As-extruded	89.3 ± 1.3	102.8 ± 0.9
Homogenized	94.6 ± 0.7	109.6 ± 1.2
HPT	121.8 ± 1.4	126.6 ± 1.5

3.2 Simulated body fluid

Simulated body fluid (SBF) was introduced by Kukubo *et al.* (1990) [66] with the concentration of ions close to human blood plasma. Since then, different types of SBF solutions have been studied for in vitro experiments. The ionic concentration of human blood plasma and SBF solutions are listed in **Table 3.3**.

Table 3.3 Ionic concentration of human blood plasma and SBFs [43].

	Ion concentration [mmol/L]							
	Na^+	K^+	Mg^{2+}	Ca^{2+}	Cl^-	HCO_3^-	HPO_4^{2-}	SO_4^{2-}
Blood plasma [42]	142.0	5.0	1.5	2.5	103.0	27.0	1.0	0.5
Original SBF	142.0	5.0	1.5	2.5	148.8	4.2	1.0	0
Corrected SBF (c-SBF)	142.0	5.0	1.5	2.5	148.8	4.2	1.0	0.5
Revised SBF (r-SBF)	142.0	5.0	1.5	2.5	103.0	27.0	1.0	0.5
Newly improved SBF (n-SBF)	142.0	5.0	1.5	2.5	103.0	4.2	1.0	0.5
SBF 27 [67]	142.0	5.0	1	2.5	109.0	27.0	1.0	1.0

All of the experiments in this thesis were carried out with SBF27 solution, which has a bicarbonate (HCO_3^-) concentration of 27 mmol/L [67]. The solution was prepared by dissolving chemical compounds of potassium chloride (KCl), sodium chloride (NaCl), sodium hydrogen chloride ($NaHCO_3$), magnesium sulfate heptahydrate ($MgSO_4*7H_2O$), calcium dichloride dihydrate ($CaCl_2*2H_2O$) and potassium dihydrogen phosphate (KH_2PO_4) into double distilled water. The stock solutions were prepared separately and the composition of stock solutions is shown in **Table 3.4**.

The pH value was adjusted to pH of 7.4 at 37 ℃ with TRIS and hydrogen chloride (HCl). TRIS, also called tris (hydroxymethyl) aminomethane or THAM, is an organic compound with the chemical formula $(HOCH_2)_3CNH_2$. This compound is commonly used as a buffer solution in biochemistry and molecular biology [68].

Table 3.4. Composition of stock solution.

Compound	Composition of stock solution [g/L]	Volume for 1L of SBF27 [mL]
KCl	59.64	5
NaCl	116.88	50
$NaHCO_3$	45.37	50
$MgSO_4*7H_2O$	49.3	5
$CaCl_2*2H_2O$	14.7	25
TRIS	121.16	50
KH_2PO_4	27.22	5

3.3 Immersion test

3.3.1 Sample preparation

For the immersion tests, the specimens were ground with different grades of SiC paper 1200, 2000, and 4000, washed with distilled water and rinsed with ethanol, then dried at room temperature.

To determine the corrosion rate, the diameter and height of each specimen were measured four times and averaged for reliability using a digital caliper and digital micrometer with a sensitivity of 0.001 mm. Then, each specimen was weighted with a laboratory electronic balance with high readability of 0.01 mg. After measuring size, each specimen was ultrasonically cleaned in absolute ethanol for 1 minute to prevent contamination.

The surface preparation procedure was done within 2 hours before the experiments to avoid surface oxidation and contamination.

3.3.2 Test procedure

The immersion test was carried out in 250 ml of SBF27 solution at 37 ± 1 ℃ with an initial pH of 7.4 for 168, 336, and 504 hours (i.e., 1, 2, and 3 weeks), respectively. The experimental setup is shown in **Figure 3.2(a)**.

The tested solution was renewed at intervals of 168 hours (1 week) for each specimen to maintain the concentration and the pH of the electrolyte. Each sample was put in a separate bottle filled with SBF and put in a water bath to maintain body temperature. At the end of the immersion period, the samples were removed from the solution and immediately washed with ethanol, and completely dried to prevent further corrosion.

The sample holder for the immersion test was made using a 3D printer. It was designed to reduce the contact area between the sample and the sample holder as much as possible, and the holder was made with a lid to prevent evaporation of the electrolyte during the experiment as shown in **Figure 3.2(b)**.

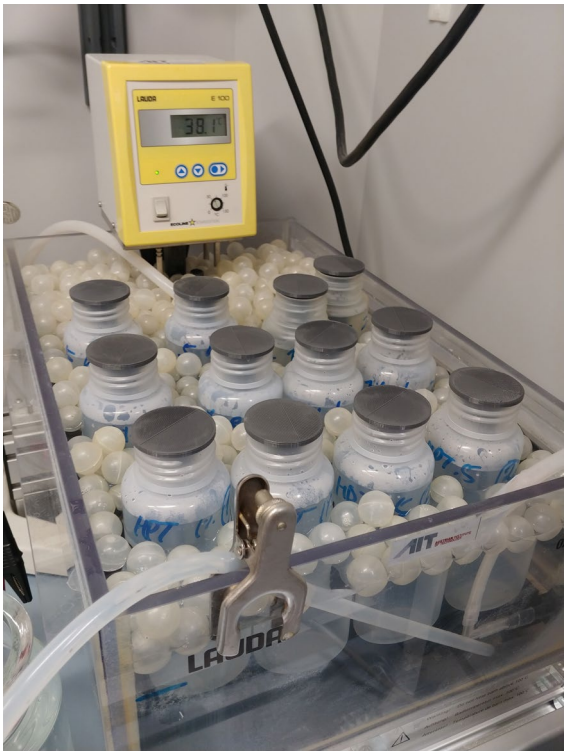

(a)

(b)

Figure 3.2. (a) Experimental setup of immersion tests. The plastic bottle with the sample inside was filled with 250 ml of SBF27 solution and placed in a thermostatic bath. The polypropylene floating balls prevent evaporation and heat loss during the experiment. (b) Schematic 3D view (left) and photo of the sample holder with a bottle (right).

To measure the amount of weight loss and determine the corrosion rate, the corrosion products are removed chemically following the method in ASTM G1-03 [56];

The corrosion products on the surface of the sample were removed in ammonium chloride (NaH_4Cl) solution (100g of NaH_4Cl with distilled water to make up 1L of chemical solution) for 3 minutes at 70 ℃, and then ultrasonically cleaned for 1 min in the NaH_4Cl solution to remove tightly adhered corrosion products. After the chemical cleaning process, the samples were rinsed with ethanol and completely dried at room temperature to measure their weight.

The weight of the sample after each cleaning cycle was recorded and plotted to determine the final weight of the sample as shown in **Figure 3.3**. Among the measured values, the final weight should be selected in the lowest slope (BC line in **Figure 3.3**) to reduce the uncertainty of the final weight by the chemical cleaning process [56].

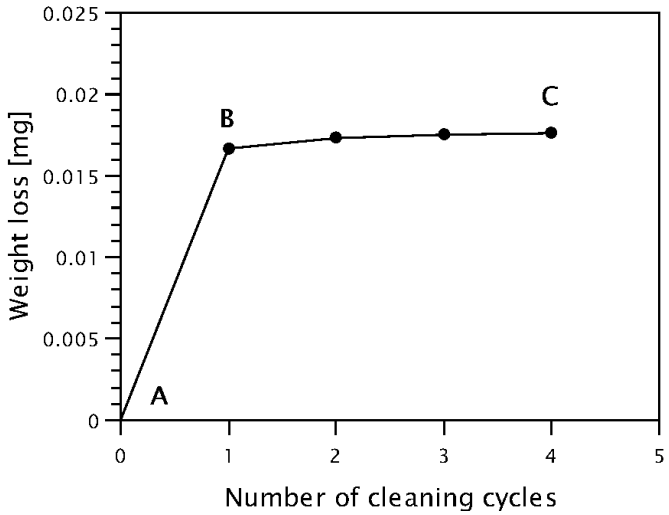

Figure 3.3. Experimental weight loss due to corrosion product removal as a function of the number of cleaning cycles.

The average weight loss per unit area was calculated by subtracting the final weight after corrosion products removal from the initial weight and divided by the exposed area, as shown below in **Equation 3.1**.

$$WL = \frac{w_i - w_f}{A} \quad (3.1)$$

where WL is the weight loss per unit area in mg/cm^2, w_i is the initial weight before immersion in mg, w_f is the final weight after immersion and corrosion products removal in mg, and A is the exposed sample surface area in cm^2.

The corrosion rates by weight loss method were calculated by the following equation [56]:

$$CR_W = K * \frac{WL}{t * d} \quad (3.2)$$

where CR_W is the corrosion rate using the weight-loss method in mm/year, K is a constant ($= 8.76 * 10^4$ for mm/year [56]) depending on the unit of corrosion rate, t is the immersion time in hours, and d is the density in g/cm^3.

After the immersion tests, the macroscopical images were taken with a digital camera before and after the corrosion products removal. In addition, light microscope images of Zn-1Mg^{hom} for different immersion times without corrosion product removal were taken for qualitative observation.

3.4 Electrochemical test

3.4.1 Sample preparation

For the electrochemical tests, the specimens were grounded with SiC paper grit of 1200, cleaned with distilled water rinsed with ethanol, and then dried at room temperature.

The disc-shaped zinc-based alloy sample was connected electrically to a PVC-coated copper wire with conductive silver-based epoxy adhesive and embedded in an epoxy resin as

illustrated in **Figure 3.4**. This was necessary to ensure that only a well-defined sample surface area is in contact with the electrolyte during the experiment.

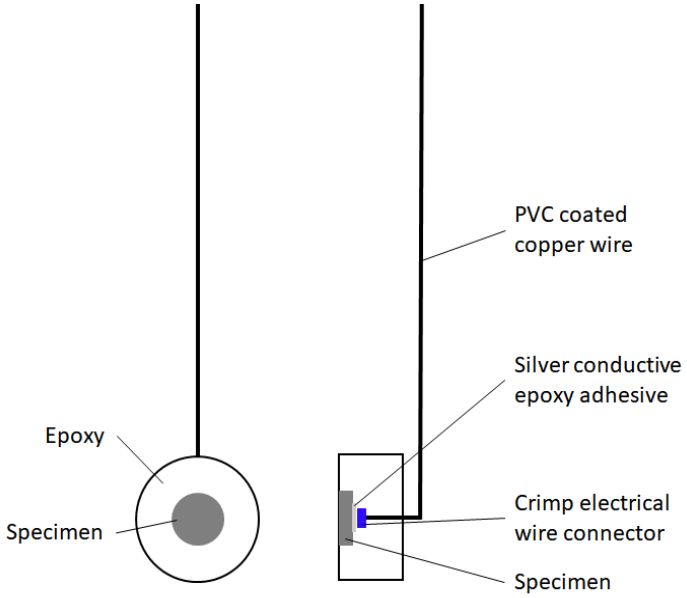

Figure 3.4. Schematic diagram of specimen for electrochemical tests.

Thereafter, the mounted sample was polished with 1200, 2000, and 4000 grit SiC papers and degreased with ethanol, then the exact surface area was measured for each specimen before testing.

3.4.2 Test procedure

The electrochemical measurements were performed in SBF27 solution at 37 ℃ with an initial pH value 7.4 using a BioLogic SP-150 potentiostat instrument and controlled by a BioLogic EC-Lab V11.36 with a standard three-electrode system with the following setup as detailed below in **Figure 3.5**:

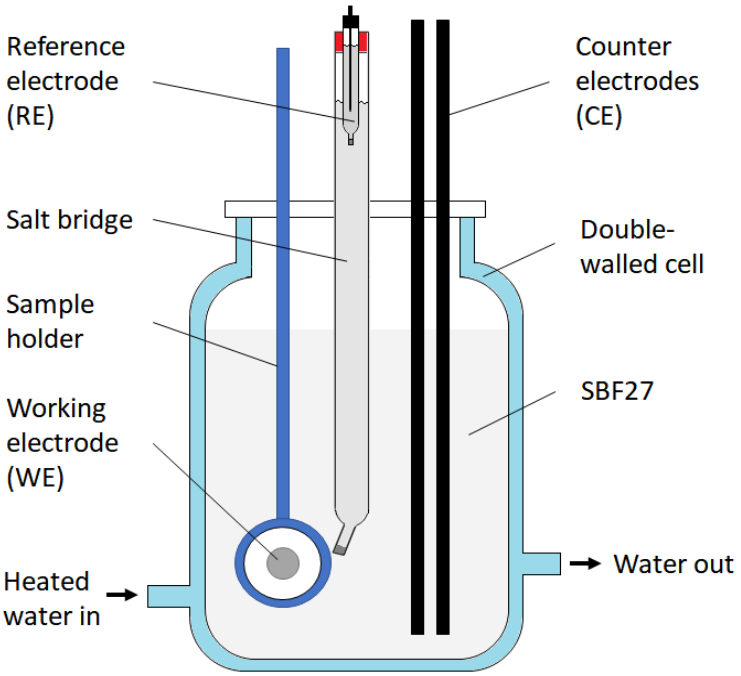

(a)

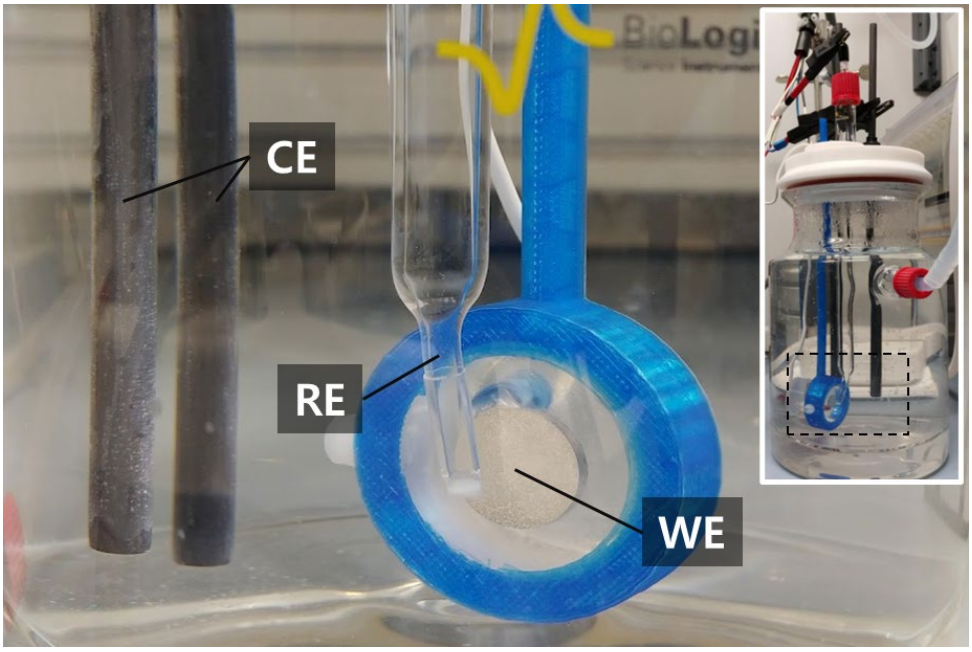

(b)

Figure 3.5 (a) Schematic setup of the standard electrochemical test cell, (b) Experimental setup used in electrochemical tests

Two graphite rods were used as the counter electrode (CE). The working electrode (WE) is the specimen with an exposed sample surface to the solution was 0.77 cm^2, approximately. As illustrated in **Figure 3.6**, the reference electrode (RE) was the silver (Ag) wire coated with silver chloride (AgCl) and immersed in 3 moles of NaCl solution. The potential of RE is 0.195 V against reversible hydrogen electrode (RHE) at 25 ℃ [70], [71].

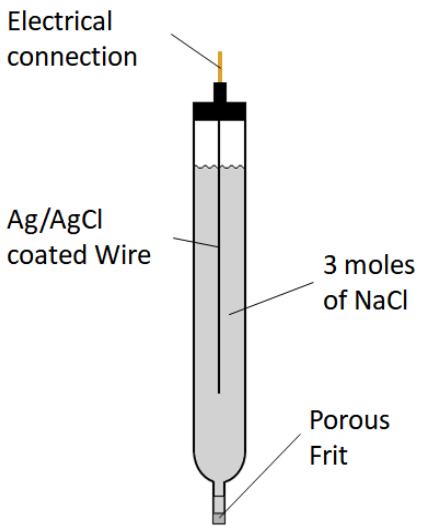

Figure 3.6. Schematic of a RE-1B Ag/AgCl reference electrode (ALS Co., Ltd, Japan).

The electrochemical measurements were carried out in a 1000 mL double jacketed glass cell connected to a water bath at 37 ℃ for temperature control.

Two measurement techniques using three-electrode electrochemical cell were performed to obtain the corrosion properties of zinc-based materials in SBF27 at 37 ± 1 ℃ with initial pH of 7.4. The following chapter describes the methods used in the electrochemical tests.

3.4.2.1 Open-circuit potential measurement

The open-circuit potential (OCP) was recorded for each sample immediately after immersion in SBF27 at 37 ± 1 ℃ with initial pH of 7.4 for 20 hours. In addition, OCPs were measured under the same condition for 5000 seconds after one week of immersion for comparison purposes.

3.4.2.2 Potentiodynamic polarization scan

The electrochemical parameters such as the corrosion potential (E_{corr}), the corrosion current density (I_{corr}), the anodic coefficient (β_a), and the cathodic coefficient (β_c) can be determined by Tafel extrapolation from the cathodic and anodic branch using the software as shown in **Figure 3.7**.

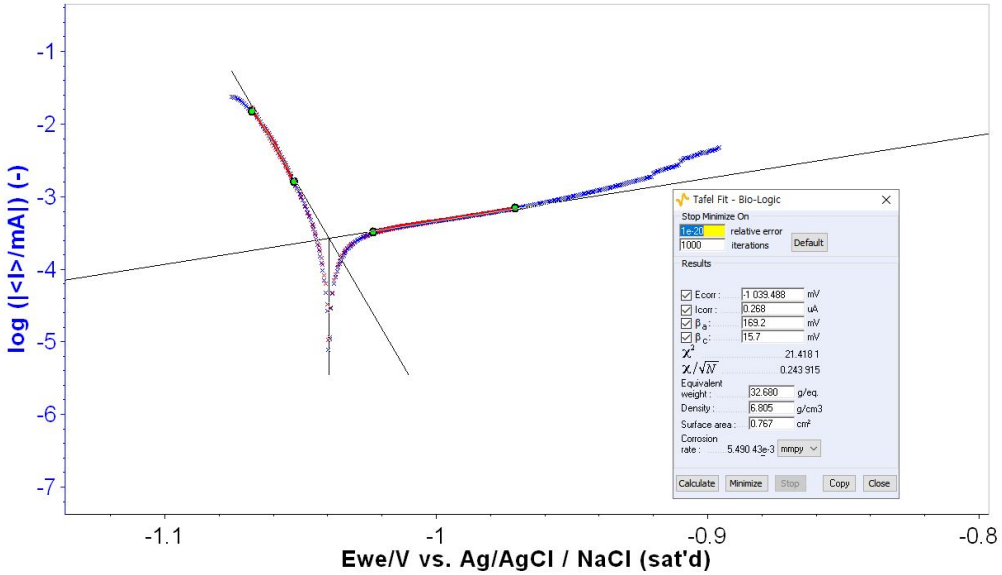

Figure 3.7. Tafel extrapolation of potentiodynamic polarization scan using the software (BioLogic EC-Lab V11.36).

The corrosion rate by electrochemical test (CR_E) was calculated using EC-LAB software as shown in **Figure 3.7** with the following equation [72]:

$$CR_E = 3.27 * 10^{-3} * \frac{I_{corr} * E.W.}{d} \quad (3.3)$$

where CR_E is the corrosion rate using the electrochemical test in mm/year, I_{corr} is the corrosion current density in $\mu A/cm^2$, E.W. is the equivalent weight in g/equivalent, d is the density in g/cm^3, and A is the exposed sample surface area in cm^2.

In most cases, only elements that consist of more than 1 weight percent of the alloy are considered in **Equation 2.16** [72]. Therefore, the equivalent weight of Zn-0.5Mg and Zn-1Mg is simply calculated using **Equation 2.15** as below

$$E.W.\ of\ Zn-0.5Mg\ and\ Zn-1Mg = \frac{65.38}{2} = 32.69$$

In this study, the PDP scan was employed to observe corrosion behavior and determine electrochemical parameters and the corrosion rate for different zinc-based alloys. Before the PDP scan, the OCP was recorded for 2000 seconds to achieve the stable potential value, and then, the PDP scan was performed $\pm$ 350 mV around the final recorded OCP at a scan rate of 0.167 mV/s based on ASTM G59-97 [76].

Chapter 4

Results

4.1 Immersion test

4.1.1 Corrosion product removal

The corrosion product removal through the chemical method using NaH_4Cl solution was performed to determine the final weight of the sample after immersion testing. However, there was an additional weight loss as the corrosion products removal process was further repeated. For this reason, to verify the amount of weight loss by the chemical cleaning, the removal procedure of the corrosion product was performed using the initial non-corroded state of the Zn-0.5Mg sample. The weight loss per unit area was calculated using **Equation 3.1**.

Figure 4.1 presents the weight loss as a function of the number of chemical cleaning cycles of the initial state of Zn-0.5Mg.

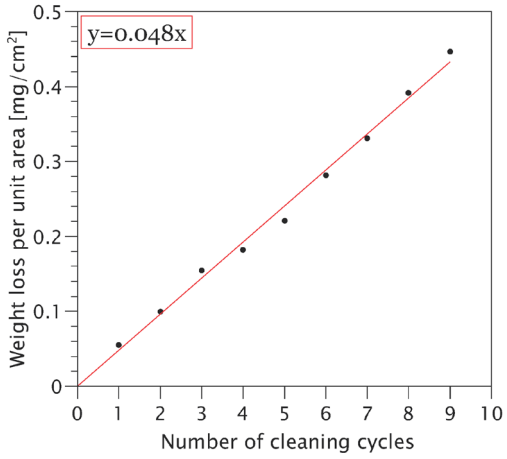

Figure 4.1. Weight loss as a function of the number of cleaning cycles of the initial state of Zn-0.5Mg.

The weight loss of the sample increased linearly during the 9 times iterative cleaning procedure. The average weight loss per unit area was 0.05 ± 0.01 mg/cm^2 at each cleaning procedure with a minimum weight loss was 0.028 mg/cm^2 at the fourth and a maximum of 0.061 mg/cm^2 at the sixth and eighth corrosion product removal process.

The red solid line in **Figure 4.1** represents the linear fit from the measured weight loss values of the sample, and the slope was determined as 0.048 mg/cm^2.

Changes in the surface of the sample were also observed by light microscopy as presented in **Figure 4.2**. As can be seen, the base materials are continuously removed by chemical cleaning procedures, and it is assumed that the preferentially dissolved substance (see **Figure 4.2(c)**) is Mg, which corrodes faster than Zn.

In this study, the corrosion product removal procedure was repeated 2 - 5 times. This means that the weight loss due to the chemical cleaning is considerably less than the total amount of weight loss caused by corrosion. However, as confirmed, the base elements were also removed to a small extent because of chemical treatment. Therefore, it should be noted that the measured weight loss of the sample after removing the corrosion products provide slightly overestimated results.

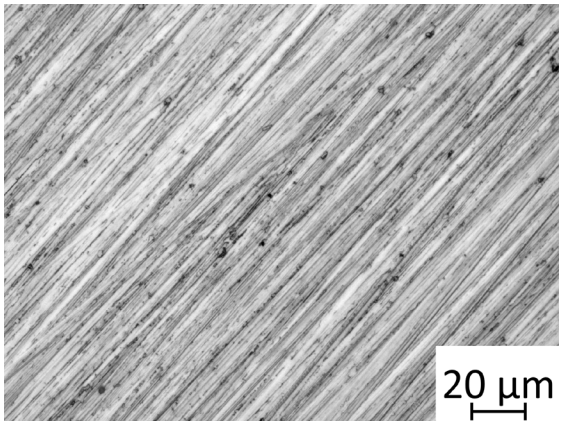

(a)

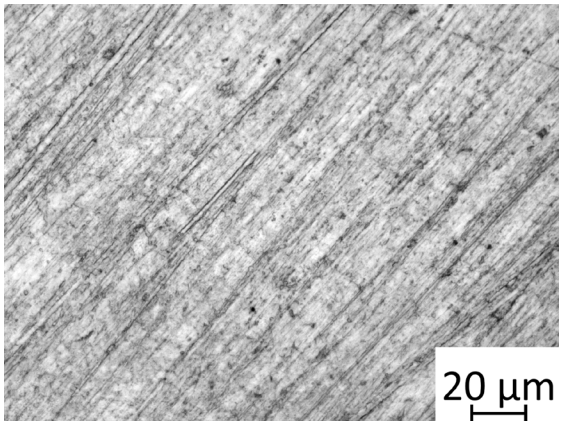

(b)

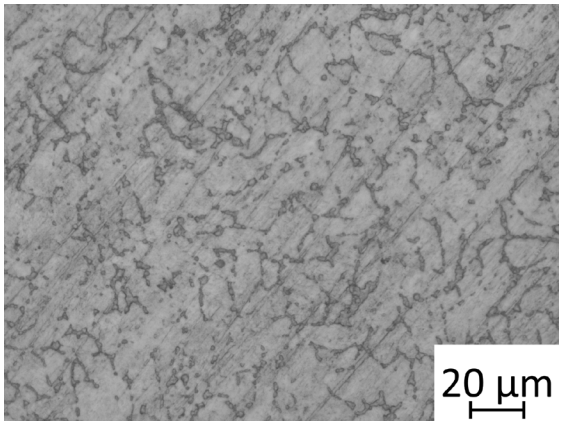

(c)

Figure 4.2 Optical microscopy images of Zn-0.5Mg after a different number of chemical cleaning cycles: (a) initial state, (b) after 4 times cleaning, and (c) after 9 times cleaning.

4.1.2 Weight loss

After corrosion product removal, the weight loss of the samples was determined. **Figure 4.3** shows experimental results of weight loss per unit area of Zn-based materials during 1, 2, and 3 weeks corresponding to 168, 336, and 504 hours in SBF27 at 37 ± 1 ℃ with an initial pH value 7.4 as a function of immersion time. Each represented value is the mean of two samples to ensure the reliability of the results for each experiment, and the error bar is the standard error. In general, it is confirmed that the average weight loss increases with increasing exposure time.

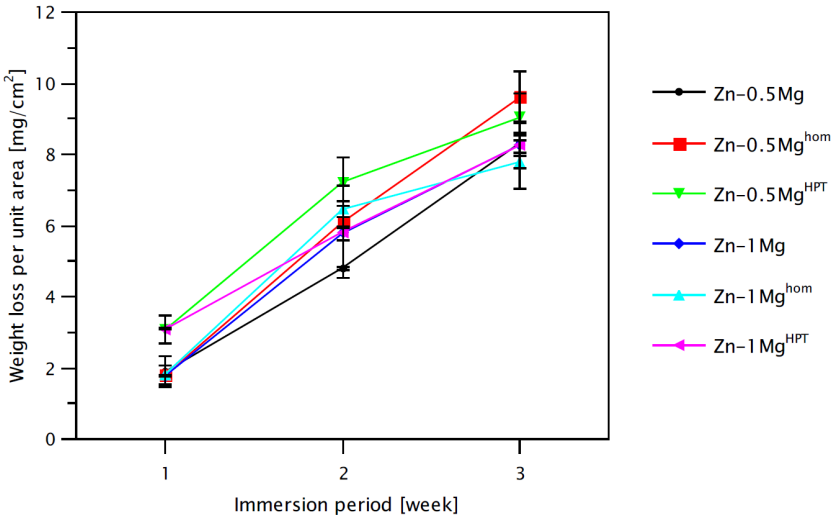

Figure 4.3. Weight loss per unit area of zinc-based materials for 1, 2, and 3 weeks in SBF27 at 37 ± 1 ℃ with an initial pH of 7.4. Represented values are the means of two samples with a standard error bar.

After 1 week of immersion, both HPT-processed samples, Zn-0.5Mg^{HPT} and Zn-1Mg^{HPT}, showed the highest weight loss per unit area with around 3.1 mg/cm^2 compared to the other samples (approximately 1.8 mg/cm^2).

After 2 weeks of immersion, the amount of weight loss increased for all samples, Zn-0.5Mg^{HPT} has the highest weight loss with 7.22 mg/cm^2, while Zn-0.5Mg showed the lowest value with 4.81 mg/cm^2.

Similarly, after 3 weeks, the weight loss of all zinc-based materials also increased as expected. The summary of average weight loss results is given in **Table 4.1**.

Table 4.1. Summary of average weight loss per unit area of zinc-based materials for 1, 2, and 3 weeks. Represented values are the means of two samples.

	1 week (168 h) [mg/cm^2]	2 weeks (336 h) [mg/cm^2]	3 weeks (504 h) [mg/cm^2]
Zn-0.5Mg	1.89 ± 0.43	4.81 ± 0.04	8.32 ± 0.28
Zn-0.5Mg^{hom}	1.79 ± 0.02	6.09 ± 0.16	9.61 ± 0.74
Zn-0.5Mg^{HPT}	3.07 ± 0.40	7.22 ± 0.69	9.04 ± 0.66
Zn-1Mg	1.77 ± 0.27	5.78 ± 0.20	8.27 ± 0.66
Zn-1Mg^{hom}	1.82 ± 0.26	6.46 ± 0.23	7.79 ± 0.76
Zn-1Mg^{HPT}	3.08 ± 0.02	5.82 ± 1.32	8.26 ± 0.29

4.1.3 Corrosion rate by immersion test for 1, 2, and 3 weeks

Figure 4.4 and **Table 4.2** present the averaged corrosion rates of investigated zinc-based materials immersed in SBF27 at 37 ± 1 ℃ with an initial pH value of 7.4 after 1, 2, and 3 weeks, respectively.

Two samples of each type of material and each immersion period were examined. The corrosion rate was calculated by the weight loss data (see **Table 4.1**) using **Equation 3.2**, according to ASTM G01 - 03 [56]. Represented values in **Figure 4.4** and **Table 4.2** are the means of two samples with a standard error bar.

The results of the corrosion rate of different Zn-based materials after 1 week of immersion are shown in **Figure 4.4(a)**. Both HPT-processed samples, Zn-0.5Mg^{HPT} and Zn-1Mg^{HPT}, showed a higher corrosion rate with about 0.24 mm/year in contrast to the other samples. The other 4 samples, Zn-0.5Mg, Zn-0.5Mg^{hom}, Zn-1Mg, and Zn-1Mg^{hom}, showed similar corrosion rates with approximately 0.14 mm/year despite having different weights percent of magnesium and

different heat treatments.

The corrosion rates after 2 weeks of immersion are presented in **Figure 4.4(b)**. It is observed that the corrosion rates of Zn-0.5Mg, Zn-0.5Mg^{hom}, Zn-0.5Mg^{HPT}, Zn-1Mg, and Zn-1Mg^{hom} increased, while Zn-1Mg^{HPT} was reduced by 1.25 % compared to the result of the 1-week immersion test. At the same Mg concentration, the homogenized sample showed a higher corrosion rate than the as-extruded samples, this may be due to the formation of an only loosely bounded corrosion product layer on the homogenized sample surface, which cannot effectively protect the sample surface from corrosion.

In most cases, the 1 wt % Mg samples had a higher corrosion rate than the 0.5 wt % Mg samples. It is obvious that Mg has a high corrosion rate; as a result, the corrosion rate increases with increasing Mg content.

The results of 3 weeks immersion test are shown in **Figure 4.4(c)**. The corrosion rate of Zn-0.5Mg and Zn-0.5Mg^{hom} progressively increased with extended exposure time after 3 weeks of immersion. By contrast, Zn-1Mg and Zn-1Mg^{hom} showed a lower corrosion rate compared to corrosion rates after two weeks of immersion. Both HPT-processed samples, Zn-0.5Mg^{HPT} and Zn-1Mg^{HPT}, showed a reduction in corrosion rates compared to the 1- and 2-weeks immersion tests.

Table 4.2. Summary of the average corrosion rate of zinc-based materials after 1, 2, and 3 weeks of immersion in SBF27 at 37 ℃ with an initial pH of 7.4

	CR_W [mm/year] after 1 week	CR_W [mm/year] after 2 weeks	CR_W [mm/year] after 3 weeks
Zn-0.5Mg	0.14 ± 0.05	0.18 ± 0.01	0.22 ± 0.01
Zn-0.5Mg^{hom}	0.14 ± 0.01	0.23 ± 0.01	0.24 ± 0.02
Zn-0.5Mg^{HPT}	0.24 ± 0.05	0.29 ± 0.04	0.23 ± 0.03
Zn-1Mg	0.14 ± 0.03	0.22 ± 0.01	0.22 ± 0.03
Zn-1Mg^{hom}	0.14 ± 0.03	0.25 ± 0.01	0.20 ± 0.02
Zn-1Mg^{HPT}	0.24 ± 0.01	0.24 ± 0.08	0.22 ± 0.01

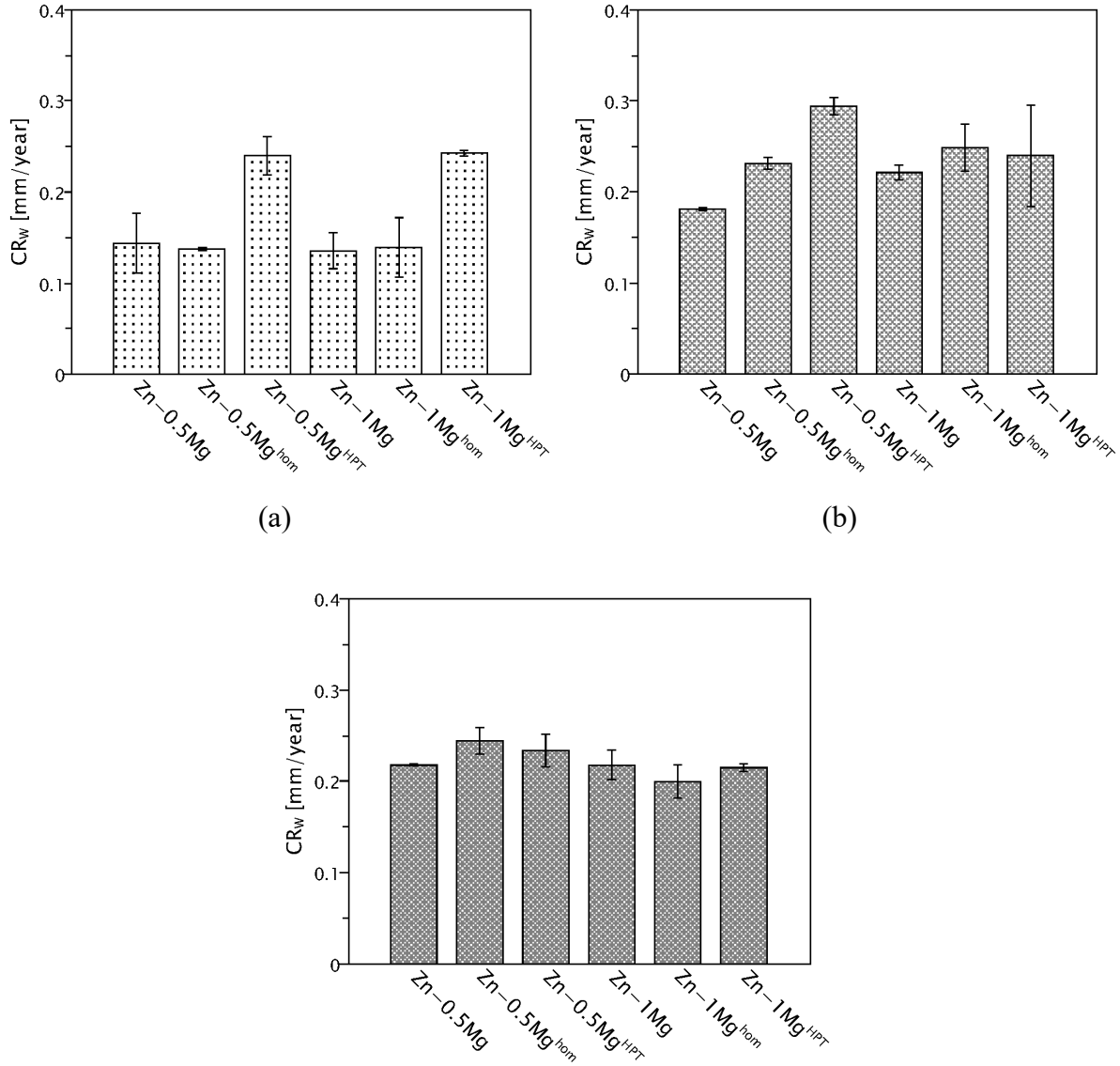

Figure 4.4. Averaged corrosion rate of Zn-Mg for (a) 1 week (168 hours), (b) 2 weeks (336 hours), and (c) 3 weeks (504 hours) of immersion in SBF27 with an initial pH of 7.4 at 37 ℃.

4.1.4 Optical macrographs

The macro corrosion morphologies of zinc-based alloys after 1, 2, and 3 weeks of immersion in SBF27 with an initial pH of 7.4 at 37 ℃ are shown in **Figure 4.5**.

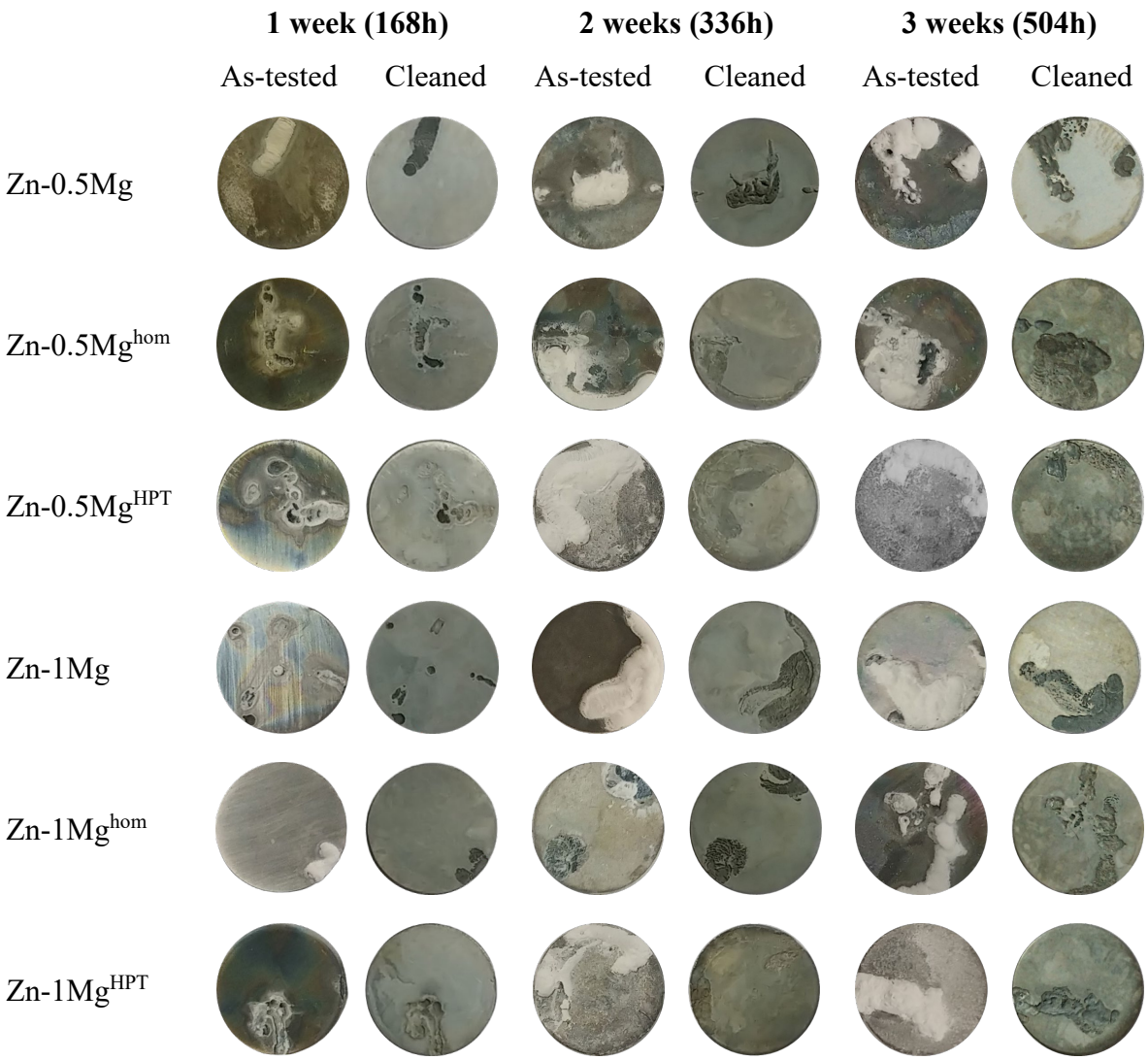

Figure 4.5. Images of tested samples after immersion in SBF27 with an initial pH of 7.4 at 37 ℃ for 1, 2, and 3 weeks before (left) and after (right) corrosion product removal.

As can be seen in **Figure 4.5**, the coverage of the surface with corrosion products increased with increasing immersion time. An accumulation of thick white corrosion products on the sample surface with increasing exposure time is also observed which is mainly formed around severe localized and pitting corrosion.

In general, a partially formed corrosion product layer was visually confirmed in most of the samples; however, both HPT-processed samples show an almost entirely formed corrosion product layer on the sample surface after 2 and 3 weeks of immersion, as shown in **Figure 4.6**. This could be due to the high grain boundary density after the HPT process [80], [81].

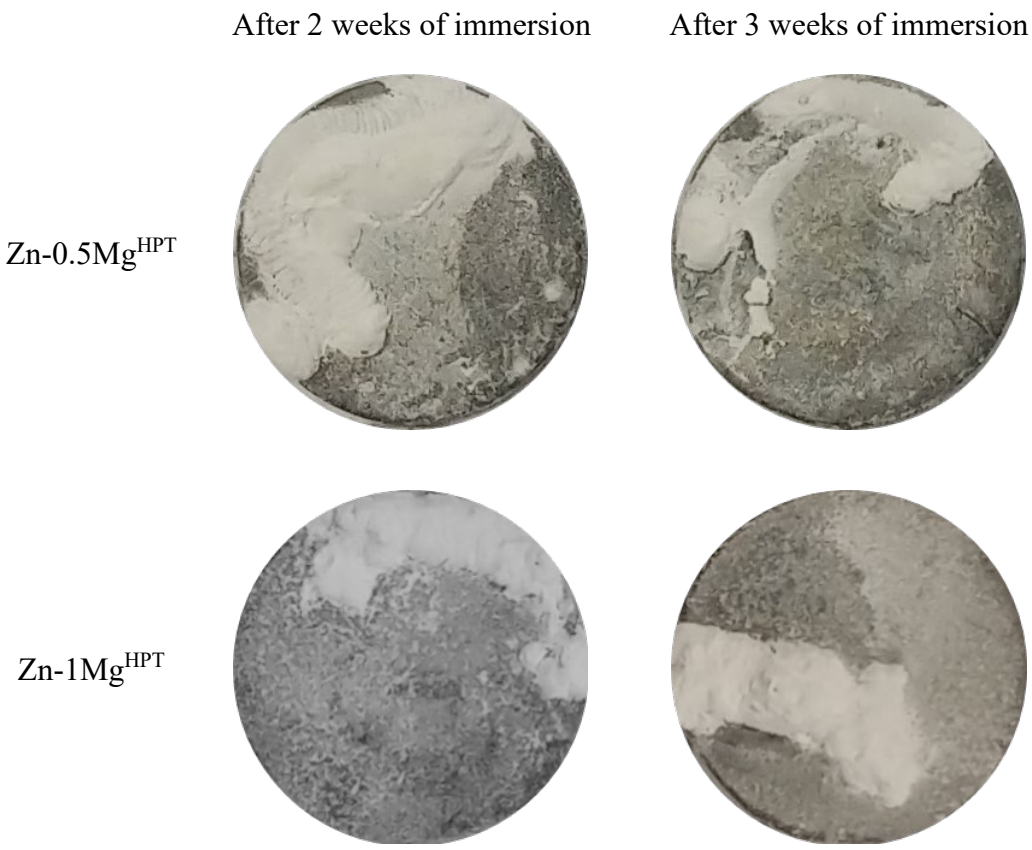

Figure 4.6. Enlarged Zn-0.5Mg^{HPT} and Zn-1Mg^{HPT} images after 2 and 3 weeks of immersion.

Interestingly, severe localized corrosion (i.e., pitting corrosion) was frequently observed at the contact area between the sample and sample holder as shown in **Figure 4.7**. It can be speculated that the formation of protective hydroxide films (i.e., $Zn(OH)_2$ and $Mg(OH)_2$) or corrosion product layer may have been hindered by the sample holder.

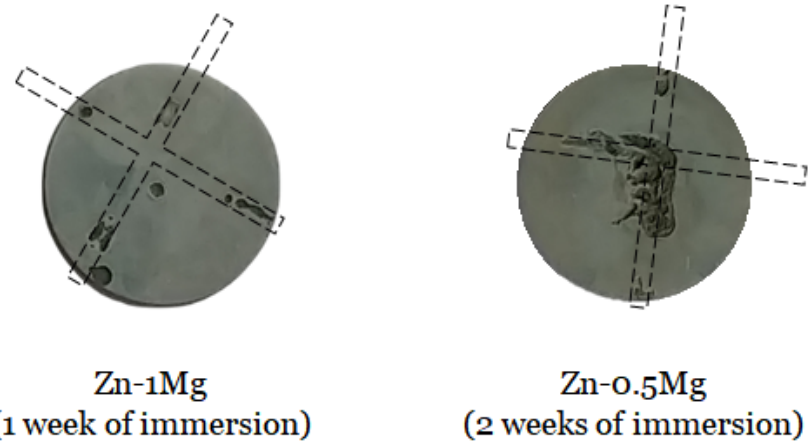

Figure 4.7. Severe localized and pitting corrosion occurred at the contact area between the sample and sample holder which is marked with a black dashed line.

Figure 4.8 contains the light microscope images of Zn-1Mg^{hom} for different immersion times before the corrosion product removal process. It could be seen that the formation of corrosion products is related to pores, which are the initial defects produced during the manufacturing process. The position of initial defects is marked with small red squares in **Figure 4.8(a)**. This occurrence indicates that the damaged area of the sample surface releases more zinc ions, leading to a thick corrosion product layer.

After 24 hours of immersion, as can be seen in **Figure 4.8(b)**, small black spots appeared on the surface due to corrosion, and further corrosion products were also visible under a light microscope as gray dots.

Figure 4.8(b) to **Figure 4.8(d)** show that the volume of the corrosion product layer on the sample surface gradually grew as the immersion time increased. After two weeks of immersion,

it was found that a dense layer of corrosion products had formed on the sample surface due to the interaction between the various ions in the SBF27 solution and the zinc and magnesium ions that were continuously released from the sample surface.

After 2 weeks of immersion, large amounts of crystallized corrosion products, which may include $Zn_3(PO_4)_2$, $Ca_3(PO_4)_2$, and $CaHPO_4 \cdot 2H_2O$, were observed on the surface, as shown in **Figure 4.8(d)**.

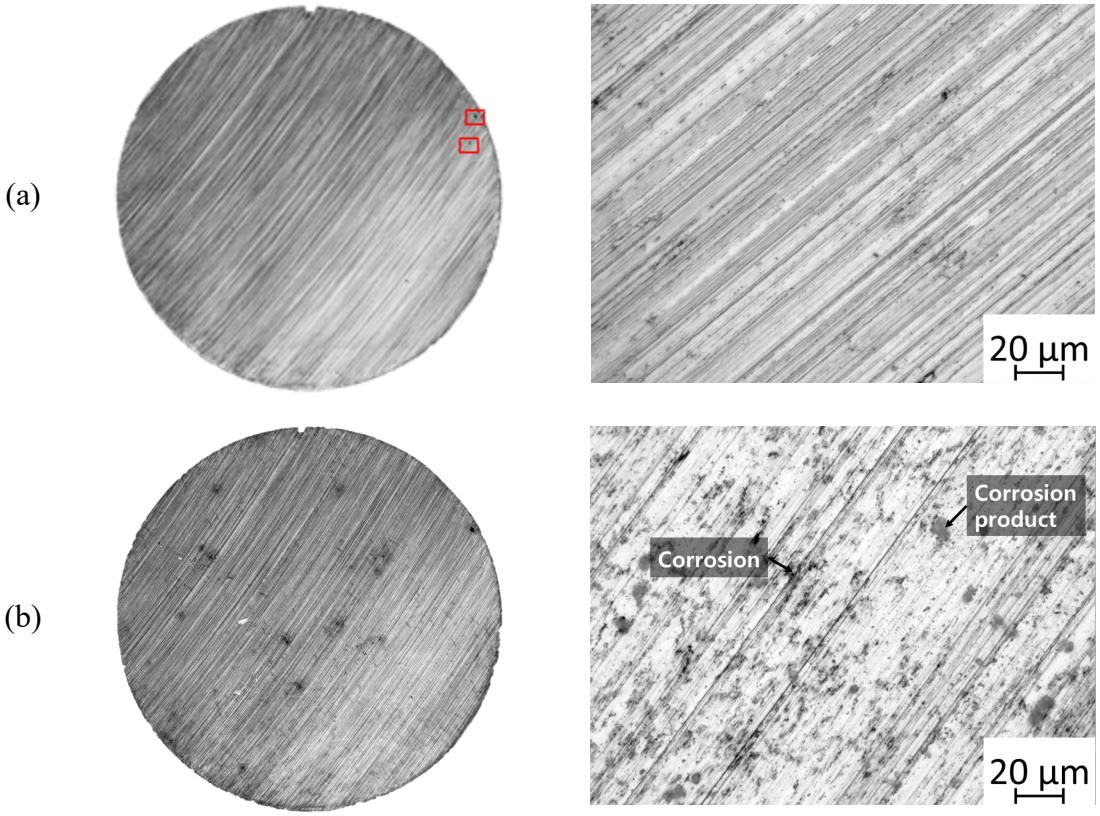

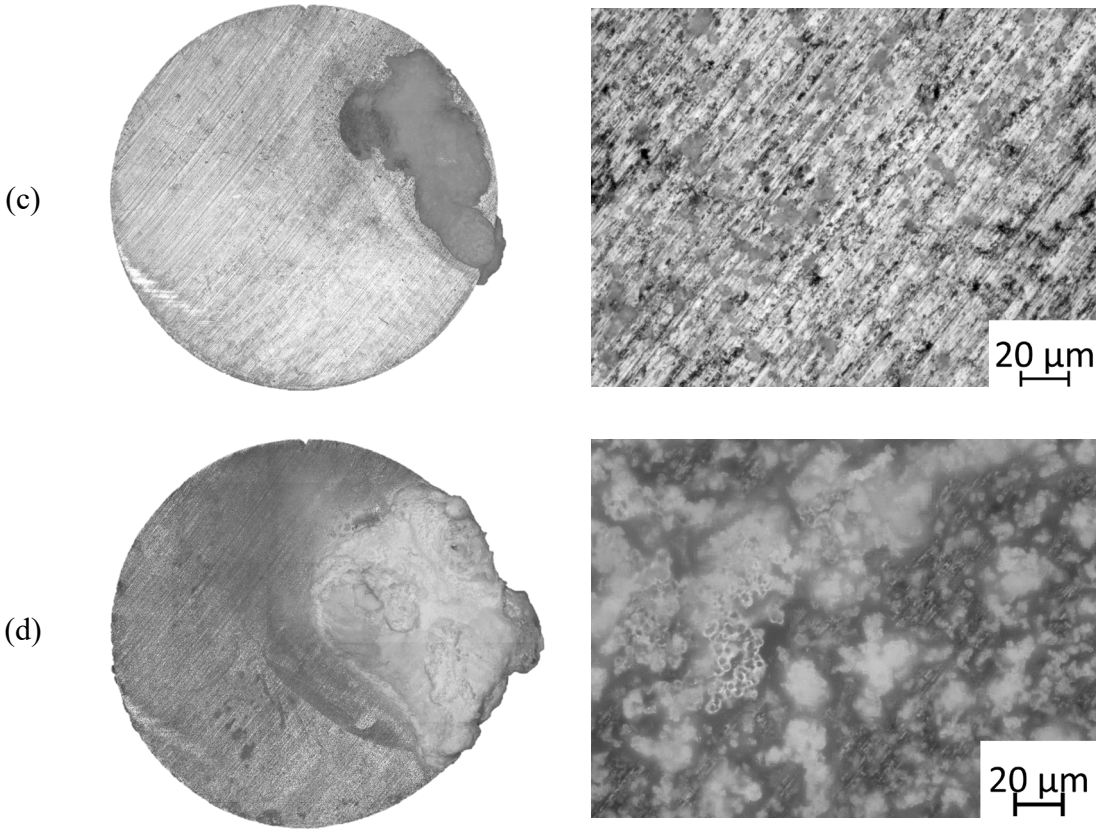

Figure 4.8. Entire sample surface (left) and high magnification (right) light microscope images of Zn-0.5Mg^{hom} immersed in SBF27 with an initial pH of 7.4 at 37 ℃ for different immersion times without corrosion products removal. (a) initial condition (defects produced during the manufacturing process are marked with red small squares), after (b) 24 hours, (c) 1 week, and (d) 2 weeks of immersion.

4.2 Electrochemical tests

4.2.1 Open circuit potential (OCP) measurements

4.2.1.1 OCP from the initial state to 20 hours

The variation of OCP (i.e., corrosion potential) of 6 different zinc-based materials in SBF27 solution at 37 $\pm$ 1 ℃ with an initial pH of 7.4 recorded during 20 hours as a function of time is shown in **Figure 4.9(a)** to **Figure 4.9(f)**.

In general, all OCPs showed a tendency to stabilize after increasing from their respective minimal values. An increase in OCP means that the material condition has become a more noble state, and this increase may be due to the decrease in Mg concentration on the surface, which has a higher corrosion rate than Zn, or it may be the result of the formation of a thin oxide or hydroxide film, such as ZnO and $Zn(OH)_2$, which protects the sample surface against the corrosion process.

After reaching a steady state, the OCP began to fluctuate. About the fluctuation range, the uncertainty of the reference electrode is around 5 mV, therefore changes below 10 mV are negligible.

The average, minimum, and maximum OCP values for different zinc-based materials are listed in **Table 4.3**.

Table 4.3. The average, minimum, and maximum open circuit potential (OCP) of zinc-based materials for 20 hours in SBF27 at 37 ℃.

	average E_{OCP} $[V_{Ag/AgCl/NaCl}]$	max E_{OCP} $[V_{Ag/AgCl/NaCl}]$	min E_{OCP} $[V_{Ag/AgCl/NaCl}]$
Zn-0.5Mg	-0.93	-0.90	-1.06
Zn-0.5Mg^{hom}	-0.91	-0.88	-1.04
Zn-0.5Mg^{HPT}	-0.97	-0.92	-1.07
Zn-1Mg	-0.91	-0.87	-1.07
Zn-1Mg^{hom}	-0.88	-0.86	-1.09
Zn-1Mg^{HPT}	-0.92	-0.86	-1.07

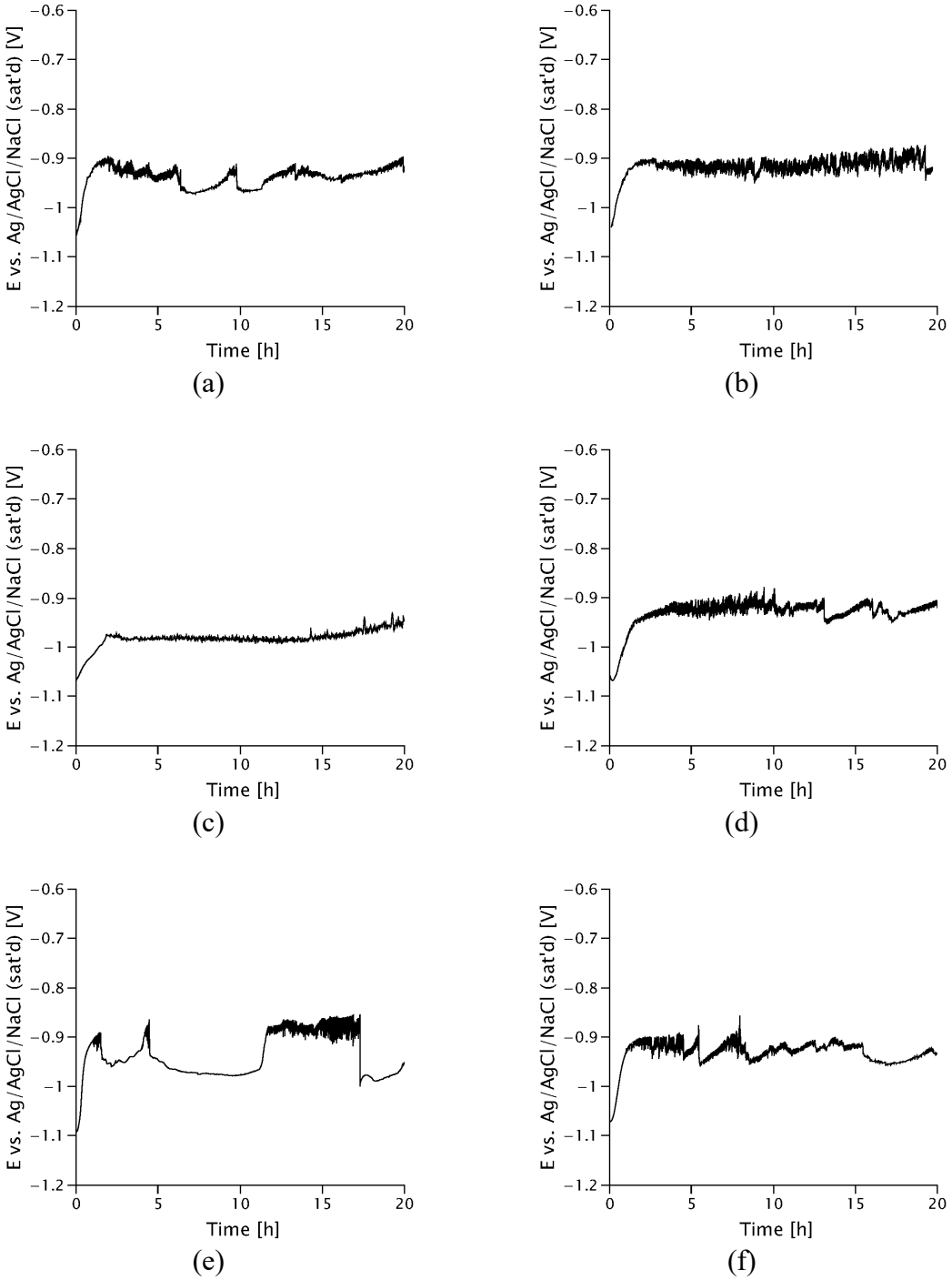

Figure 4.9. Open circuit potential (OCP) of different zinc-based materials for 20 hours in SBF27 with an initial pH of 7.4 at 37 ℃: (a) Zn-0.5Mg, (b) Zn-0.5Mg^{hom}, (c) Zn-0.5Mg^{HPT}, (d) Zn-1Mg, (e) Zn-1Mg^{hom}, and (f) Zn-1Mg^{HPT}

According to one interesting finding about OCP fluctuation by Hashimoto, M., Miyajima, S., and Murata, T. (1992) [82], this potential fluctuation can be related to the breakdown and restoration of the protective passive film on the surface. They explained that the OCP fluctuation of iron consists of four steps: (1) pit nucleation, (2) start of pit growth, (3) end of pit growth, and (4) pit repassivation. A schematic representation of this process is shown below in **Figure 4.10**.

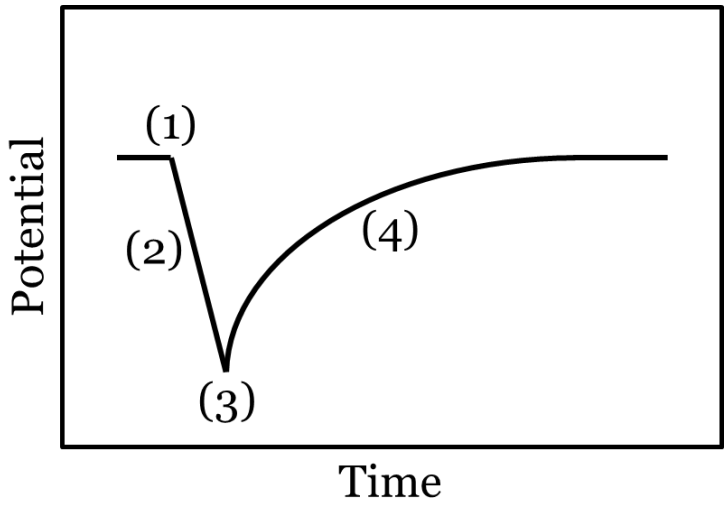

Figure 4.10. Open circuit potential (OCP) fluctuation is due to the pitting process: (1) pit nucleation, (2) start of pit growth, (3) end of pit growth, and (4) pit repassivation. (Based on reference [82])

This fluctuation could also relate to local changes in pH, and the concentration of the chemical compounds in the electrolyte. In particular, surface conditions including the formation of air bubbles, the creation and dissolution of the hydroxide protective film, and the corrosion product layer can be related to this fluctuation.

4.2.1.2 OCP comparison of the initial state and after one week of immersion

Figure 4.11 shows the OCP of different zinc-based materials in their initial state and after one week of immersion in SBF27 with an initial pH of 7.4 at 37 ℃. Each state was recorded for 5000 seconds for comparison purposes.

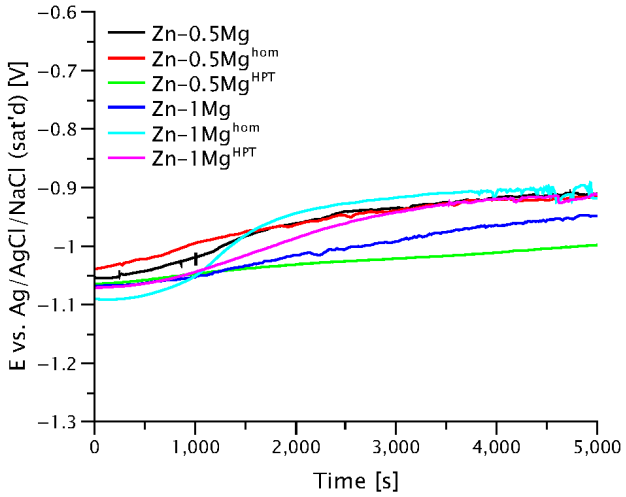

(a)

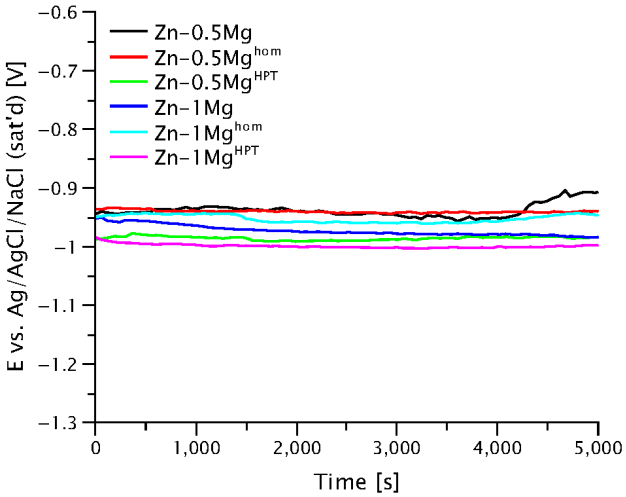

(b)

Figure 4.11. Open circuit potential of (a) initial state and (b) after 1 week of immersion of zinc-based materials in SBF27 at 37 ℃ with an initial pH of 7.4 recorded for 5000 seconds.

As discussed in the previous chapter, due to the formation of a hydroxide film on the surface, which protects the sample from corrosion, the OCP of the initial state increased over time from the minimum value of each sample and asymptotically approached the steady state. The observed average initial state of OCP values were in the following order: Zn-0.5Mg^{HPT} < Zn-1Mg < Zn-1Mg^{HPT} < Zn-0.5Mg < Zn-0.5Mg^{hom} < Zn-1Mg^{hom}. **Table 4.4(a)** summarizes the average, minimum, and maximum OCP values for the initial state alloys for 5000 seconds (= 1.4 hours).

After 1 week of immersion, both HPT-processed samples demonstrated relatively low OCP values during the steady state, indicating that they are in a more active state than other samples, and this finding agrees with the results of the 1 week of immersion test. The observed average OCPs after one week of immersion were in the following order: Zn-1Mg^{HPT} < Zn-0.5Mg^{HPT} < Zn-1Mg < Zn-1Mg^{hom} < Zn-0.5Mg^{hom} < Zn-0.5Mg. The average, minimum, and maximum OCP values after one week of immersion for different zinc-based alloys for 5000 seconds are summarized in **Table 4.4(b)**.

Generally, OCP after 1 week of immersion was more stable than the initial state, which may be because the sample has already reached a steady state. Moreover, except Zn-1Mg^{hom} and Zn-1Mg^{HPT}, average OCPs were found to be slightly higher for each sample after one week of exposure. It can be assumed that this is due to the formation of the protective layer on the sample surface.

Table 4.4. The average, minimum, and maximum open circuit potential (OCP) of zinc-based materials for 5000 seconds in SBF27 with an initial pH of 7.4 at 37 ℃: (a) initial state and (b) after 1 week of immersion

(a)

	average E_{OCP} [$V_{Ag/AgCl/NaCl}$]	max E_{OCP} [$V_{Ag/AgCl/NaCl}$]	min E_{OCP} [$V_{Ag/AgCl/NaCl}$]
Zn-0.5Mg	-0.961	-0.910	-1.055
Zn-0.5Mg^{hom}	-0.959	-0.915	-1.039
Zn-0.5Mg^{HPT}	-1.029	-0.998	-1.065
Zn-1Mg	-0.998	-0.947	-1.068
Zn-1Mg^{hom}	-0.926	-0.894	-1.092
Zn-1Mg^{HPT}	-0.969	-0.911	-1.071

(b)

	average E_{OCP} [$V_{Ag/AgCl/NaCl}$]	max E_{OCP} [$V_{Ag/AgCl/NaCl}$]	min E_{OCP} [$V_{Ag/AgCl/NaCl}$]
Zn-0.5Mg	-0.938	-0.904	-0.957
Zn-0.5Mg^{hom}	-0.940	-0.934	-0.944
Zn-0.5Mg^{HPT}	-0.986	-0.977	-0.991
Zn-1Mg	-0.973	-0.950	-0.985
Zn-1Mg^{hom}	-0.952	-0.943	-0.961
Zn-1Mg^{HPT}	-0.999	-0.984	-1.003

4.2.2 Potentiodynamic potential (PDP) measurements

Figure 4.12 shows PDP curves of the initial state of investigated zinc-based materials in SBF27 at 37 ± 1℃ with an initial pH value of 7.4. Before the PDP scan, OCP was measured for 2000 seconds to reach E_{OCP} at a steady state.

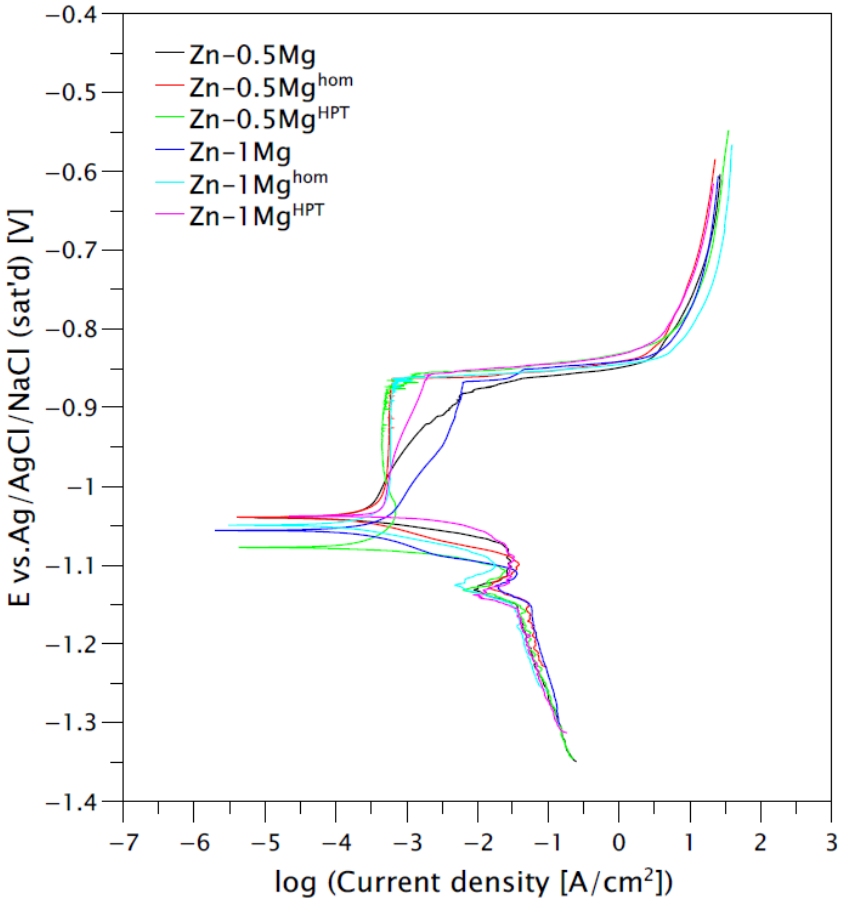

Figure 4.12. Potentiodynamic polarization (PDP) scans of studied materials in SBF27 at 37 ℃ with an initial pH of 7.4.

The results of the PDP scans reveal a similar behavior for all samples.

In the active region, the cathodic branch had an unexplainable measured current density drop at around -1.15 $V_{Ag/AgCl/NaCl}$. This could be due to either the cathodic reactions slowing, or the

anodic reactions increasing. Afterward, the corrosion potential (E_{corr}) is reached where the measured current passes through zero in the PDP scan. Theoretically, this potential should be close to the measured OCP, however, the measured E_{corr} was lower than the OCPs for all samples.

Above E_{corr}, the observed current density strongly increased with increasing applied potential. However, it then rolled off within a potential range roughly from -1.05 $V_{Ag/AgCl/NaCl}$ to -0.85 $V_{Ag/AgCl/NaCl}$ due to the formation of the protective hydroxide film (i.e., $Zn(OH)_2$ and $Mg(OH)_2$) on the sample surface. This region is called the passive region.

In the transpassive region, where the passive film broke down, a sharp increase in current density can be seen, and the oxygen gas began to evolve, as the applied potential increased on the sample surface. Then, rapid dissolution of material was observed on the sample surface as shown in **Figure 4.13**. Since pitting corrosion was observed, the potential where a rapid increase in current appeared can be defined as the pitting potential (E_{pit}). It is around -0.85 $V_{Ag/AgCl/NaCl}$ for all samples.

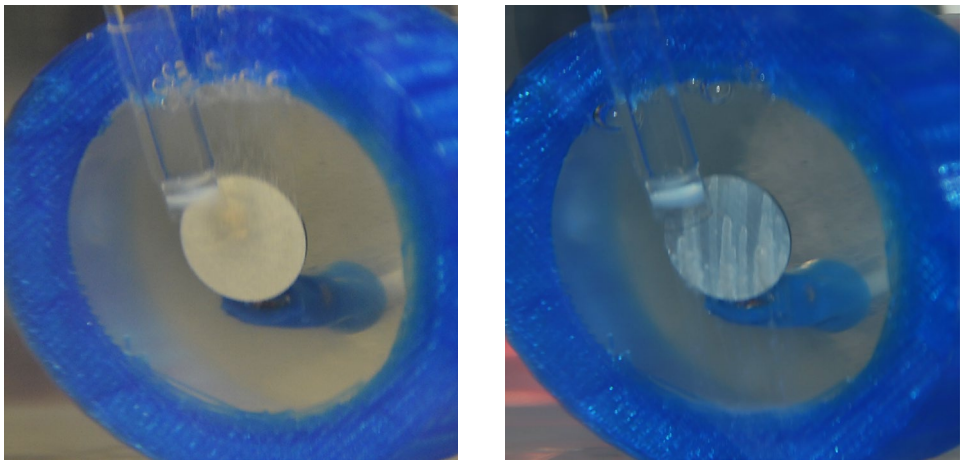

Figure 4.13. Generation of oxygen gas (left) and dissolution of the sample (right) during the potentiodynamic polarization scan.

Table 4.5 provides a summary of pitting potential (E_{pit}), corrosion potential (E_{corr}), corrosion current density (I_{corr}), Tafel slopes (β_α and β_c), and corrosion rates by electrochemical test (CR_E) using Tafel extrapolation method. **Figure 4.14** shows Tafel fit used to determine the parameters.

Table 4.5. Pitting potentials (E_{pit}), corrosion potentials (E_{corr}), corrosion current densities (I_{corr}), anodic Tafel constant (β_a), cathodic Tafel constant (β_c), and corrosion rates (CR_E) by electrochemical test determined by the Tafel extrapolation.

Materials	E_{pit} [$V_{Ag/AgCl/NaCl}$]	E_{corr} [$V_{Ag/AgCl/NaCl}$]	I_{corr} [μA]	β_a [$mV_{Ag/AgCl/NaCl}$]	β_c [$mV_{Ag/AgCl/NaCl}$]	CR_E [10^{-3} mm/year]
Zn-0.5Mg	-0.863	-1.040	0.268	171.0	15.1	5.49
Zn-0.5Mg^{hom}	-0.855	-1.050	0.475	1425.4	21.3	9.66
Zn-0.5Mg^{HPT}	-0.848	-1.078	0.380	1619.2	11.2	7.78
Zn-1Mg	-0.854	-1.074	0.493	160.4	17.2	10.17
Zn-1Mg^{hom}	-0.851	-1.052	0.546	3149.1	26.9	11.12
Zn-1Mg^{HPT}	-0.848	-1.036	0.446	433.1	9.8	9.07

Overall, the calculated corrosion rate using Tafel extrapolation indicated that the 1 wt % Mg alloy showed a higher corrosion rate than the alloy containing 0.5 wt % of Mg. However, these experimental results are less reliable due to the high variability of the electrochemical test.

Compared to the immersion test, the corrosion rates calculated from the electrochemical test were more than 40 times lower. There are several reasons which may explain this phenomenon. Firstly, the immersion test measures the overall corrosion rate over a long period, whereas the electrochemical test measures an instantaneous corrosion rate. Secondly, the electrochemical test is an accelerated experiment by the external driving force (i.e., external potential), so the results cannot be the same. Thirdly, as can be seen in **Figure 4.14**, the potential range of Tafel extrapolation is difficult to choose from measured experimental data, and it was smaller than the typical potential range for other materials.

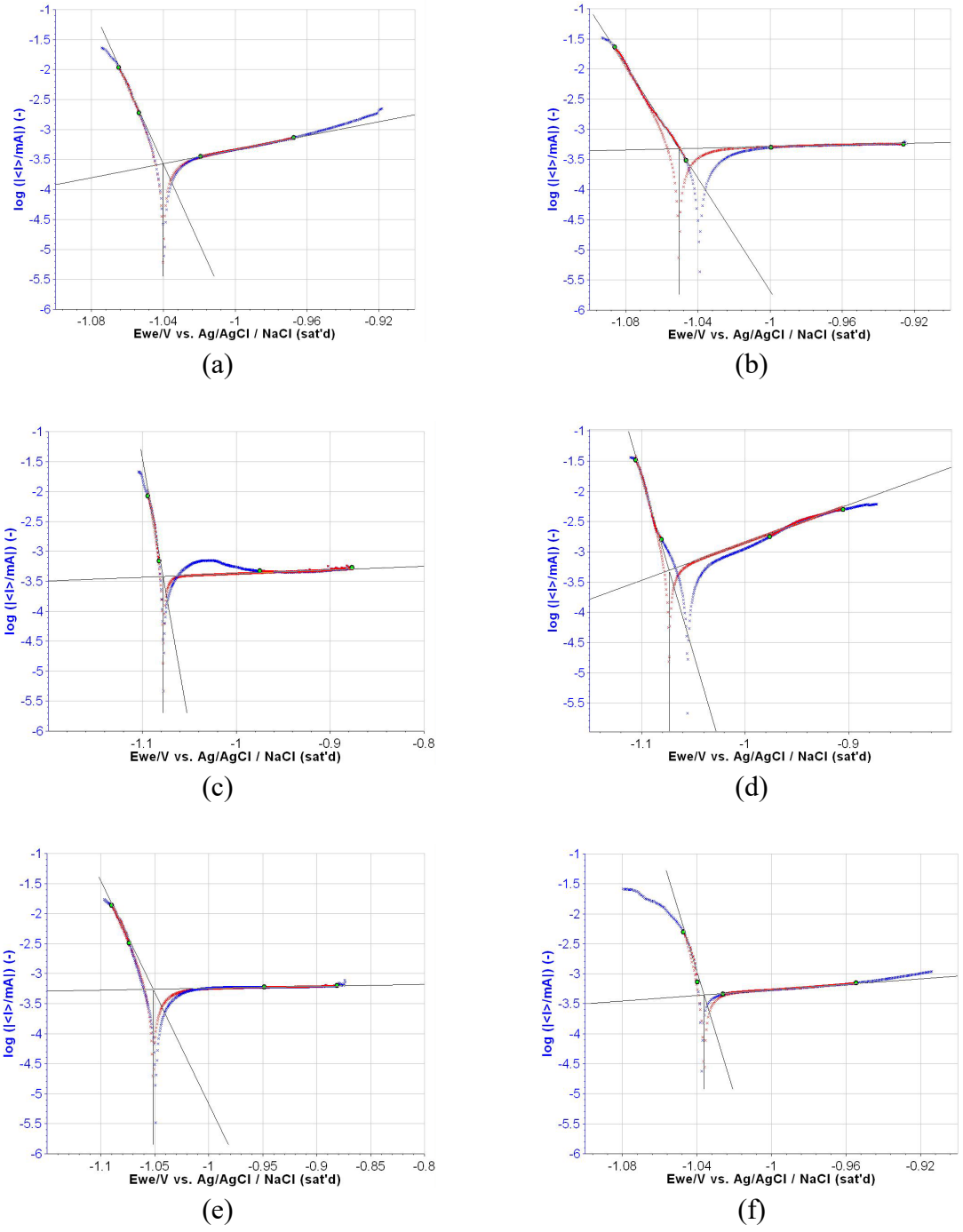

Figure 4.14. Tafel fit of (a) Zn-0.5Mg, (b) Zn-0.5Mg^{hom}, (c) Zn-0.5Mg^{HPT}, (d) Zn-1Mg, (e) Zn-1Mg^{hom}, and (f) Zn-1Mg^{HPT} in SBF27 of pH 7.4 at 37 ℃: Blue points = measured current, green points = selected fitting regions, red points = fitted Tafel line, and black solid line = Extrapolated anodic and cathodic Tafel line.

Chapter 5

Discussion

5.1 Immersion tests

5.1.1 The corrosion rate of HPT-processed samples

In the case of Mg and its alloys, there are some contradictory conclusions on the corrosion behavior after the HPT process; According to Silva, C.L.P. *et al*. (2019) [77], HPT-processing has a negligible effect on the electrochemical corrosion behavior of Mg-based alloys in a saline solution, but they also reported that the HPT process improved the corrosion resistance of pure Mg. Lopes, D.R. *et al*. (2019) [78] observed a similar influence of the HPT process on pure Mg as well as on Mg-based alloys in Hank's solution and concluded that HPT-processing may be performed to improve the corrosion resistance of Mg and its alloys. Ojdanic, A. *et al*. (2020) [85] studied the corrosion rate of HPT-processed Mg-based alloys in SBF27 solution using the hydrogen evaluation method and reported that HPT-processing slightly increases the corrosion rate of Mg5Zn, while it has no detectable influence on the corrosion rate of Mg0.3Ca. In the case of the ternary alloy Mg5Zn0.3Ca, HPT results in an increased corrosion rate in the first week and a decreased one in the third week of testing. It is concluded that mainly the composition of the alloy determines the corrosion rate.

The effects of HPT-processing on the corrosion behavior of pure Zn and Zn-based alloys in a physiological environment are not yet known in detail due to the lack of research.

Based on the research by Osório, W.R *et al*. (2005) [80], the higher grain boundary density produced by the HPT process, may result in more places for corrosion to occur, which would raise the corrosion rate. Recently, Huang, S. *et al*. (2021) [81] reported a similar effect; they concluded that the nucleation of localized corrosion, such as pitting corrosion, tends to occur more frequently at the grain boundary sites as presented in **Figure 5.1**. Therefore, maybe this

increased number of nucleation sites is another reason for the increased corrosion rate of HPT-processed Zn-0.5Mg and Zn-1Mg after one week of immersion when compared to as-extruded and homogenized samples (see **Figure 4.4(a)**).

However, as shown in **Figure 4.4(b)** and **Figure 4.4(c)**, with increased immersion time, this effect becomes less important and the corrosion rate of HPT-processed samples is similar to those of the other conditions investigated.

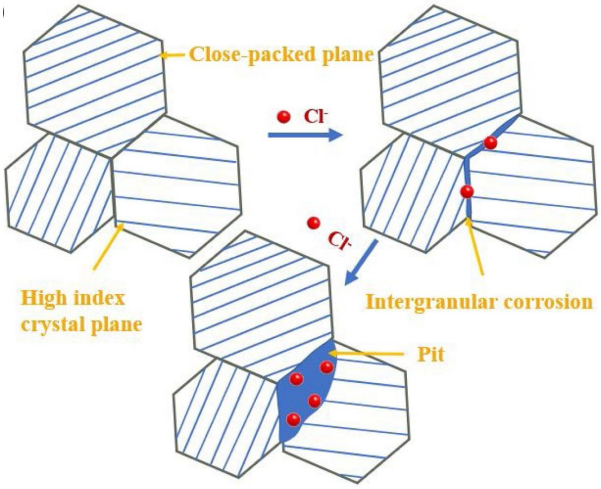

Figure 5.1. Nucleation of localized corrosion at grain boundary after the HPT process [81].

5.1.2 Corrosion rate after long-term exposure

The results after 3 weeks of immersion indicated relatively similar corrosion rates for all sample types, as shown in **Figure 4.4(c)**. It is assumed that the most important factor in corrosion behavior for long-term exposure is the accumulation of a corrosion product layer on the sample surface which is more affected by the test solution than the sample itself. Therefore, the corrosion product layer may have led to similar corrosion rates in all samples despite the different Mg concentrations and material states.

5.2 Electrochemical tests

5.2.1. The corrosion rate of HPT-processed samples

As shown in **Figure 4.9** and **Figure 4.11**, it was confirmed that both HPT-processed samples had relatively lower OCP values compared to other samples. Theoretically, a lower OCP indicates a more active state, which means that the corrosion rates of the HPT-processed samples are higher than those of all other samples.

The faster dissolution of HPT-processed samples was confirmed by a one-week immersion test. Therefore, this phenomenon could be explained by increased grain boundary density as discussed in **Chapter 5.1**.

5.2.2. Current density drop in the cathodic branch

As presented in **Figure 4.12**, an abrupt current density drop in the cathodic branch at around -1.15 $V_{Ag/AgCl/NaCl}$ was observed in all samples by PDP scan. Around this potential at a pH value of 7.4, Zn is stable, but Mg is being preferentially removed from the sample surface according to the respective Pourbaix diagrams as shown in **Figure 5.2** and **Figure 5.3**. The state corresponding to the described condition is in both cases marked with a red star. There are a few things to note here; first, the potential value -1.15 $V_{Ag/AgCl/NaCl}$ is converted to -0.96 V_{SHE} (voltage against silver chloride reference electrode use in the experiments to voltage against standard hydrogen electrode, respectively).

However, this calculation contains a small error because the reference electrode potential varies because of the temperature of the medium. Second, the local pH value can be slightly changed due to electrochemical reactions between the sample and solution. Third, although the Zn-Mg alloy reaction studied in SBF27 at 37 ℃ differs from the presented Pourbaix diagrams because they were measured in water at 25 ℃, they can be used to investigate how the material reacts in electrochemical environment.

Therefore, it can be estimated that this drop in the cathodic branch is caused by an anodic current density increasing due to the dissolution of Mg on the sample surface.

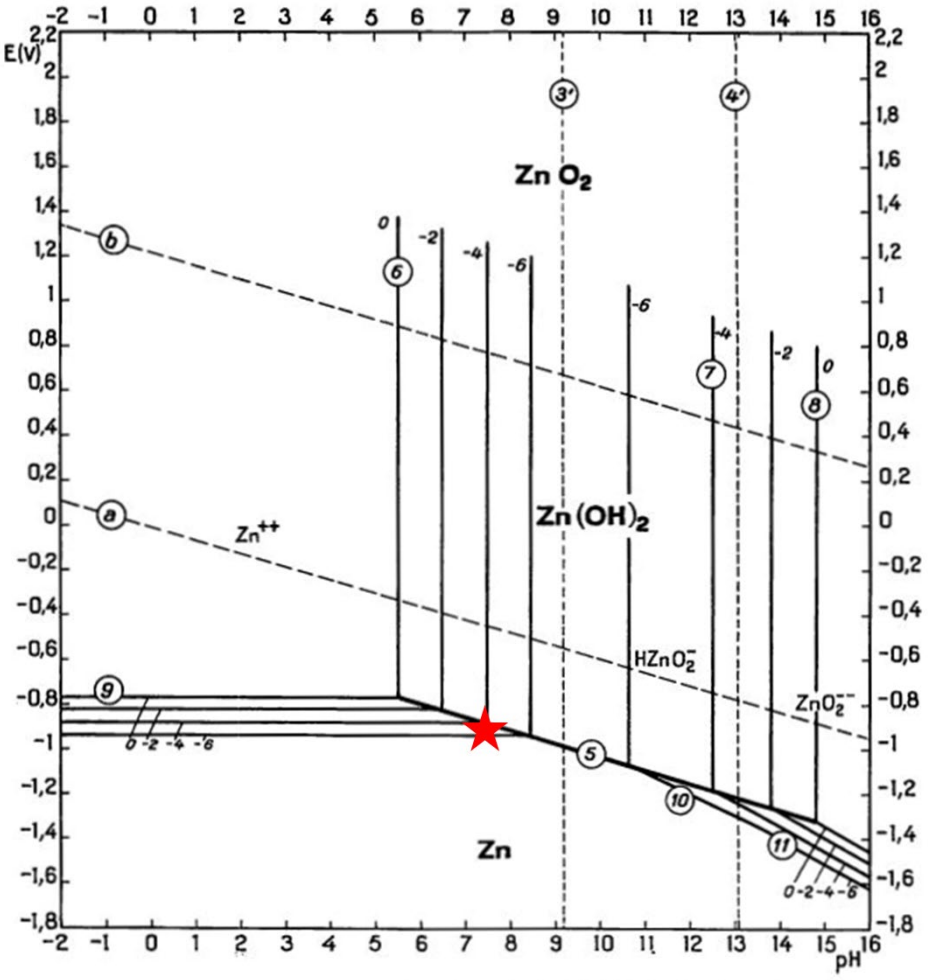

Figure 5.2. Pourbaix diagram for the system zinc-water at 25 ℃ [74]. The position of red stars corresponds to the current density drop in the cathodic branch as shown in **Figure 4.13**.

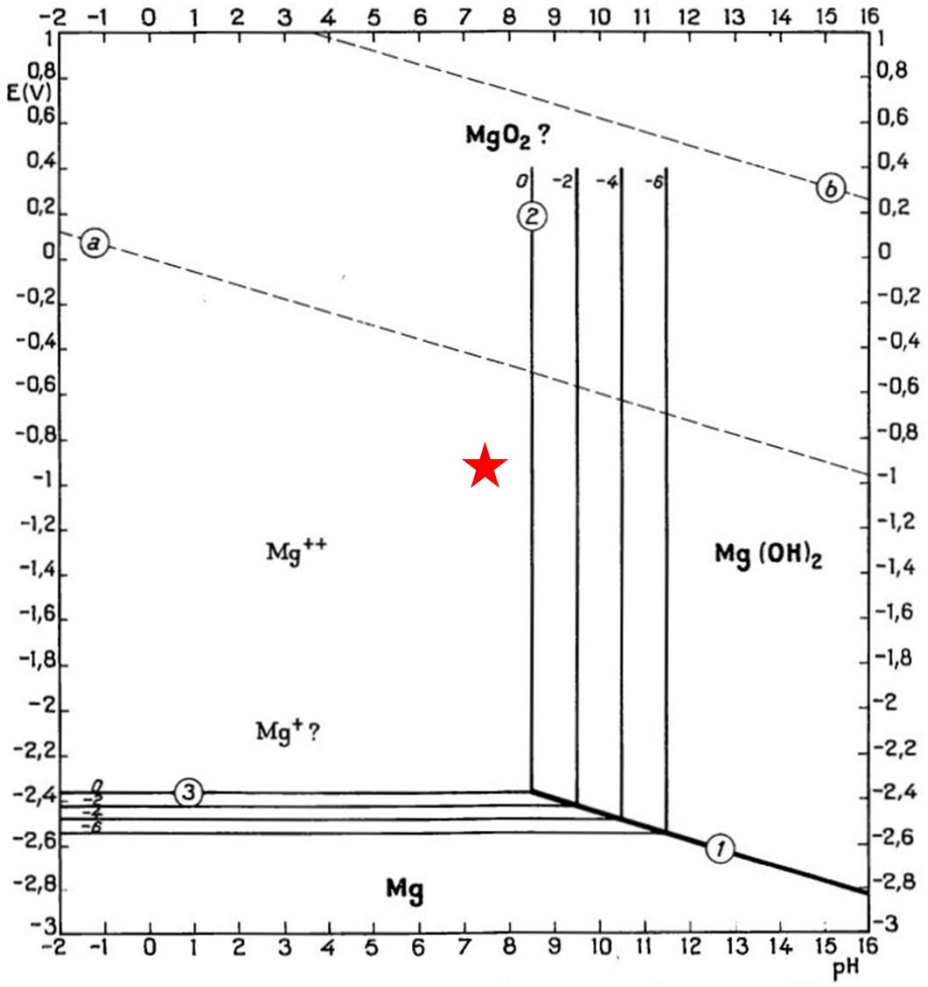

Figure 5.3. Pourbaix diagram for the system magnesium-water at 25 ℃ [74]. The position of red stars corresponds to the current density drop in the cathodic branch as shown in **Figure 4.13**.

Chapter 6
Summary and outlook

Biodegradable metals (i.e., Fe, Mg, and Zn) are suggested as potential materials for temporary medical devices like vascular stents and orthopedic implants for fixing fractured bones. However, the very low and very high corrosion rates of Fe and Mg, respectively, are not suitable for several medical applications; that is why recently zinc and zinc-based alloys with medium corrosion rates have been attracting increasing attention.

In the present work, the *in vitro* corrosion behavior of Zn-Mg alloys with different Mg contents of 0.5 and 1 wt % under three different processing procedures: (i) extrusion, (ii) extrusion + homogenization, and (iii) extrusion + homogenization + High-Pressure Torsion (HPT), has been investigated via immersion tests and electrochemical measurements in simulated body fluid (SBF27) at 37 ℃ with an initial pH value of 7.4. Here, the homogenization and processing method of HPT have been applied in order to improve the mechanical properties of Zn-Mg alloys.

The immersion tests were performed for 1, 2, and 3 weeks, and the weight loss method was conducted to determine the corrosion rates of the studied materials. Moreover, optical images and surface topographies have been taken using a digital camera and light microscopy for qualitative observation.

Higher corrosion rates of both HPT-processed samples (0.24 mm/year) were observed compared to the other samples (0.14 mm/year) after one week of immersion. This result is assumed to be due to the influence of the increased grain boundary density formed by HPT-processing. After three weeks of immersion, the corrosion rates were similar in all samples (0.22 - 0.24 mm/year). This may be because of the influence of accumulated corrosion product layer on the sample surface which protects the sample from further strong corrosion and which is rather depends on the environment than on the sample's composition and/or microstructure.

Electrochemical corrosion behavior was studied by open circuit potential (OCP) measurements and potentiodynamic polarization (PDP) scans. The results of OCP measurements showed that both HPT-processed samples exhibited comparatively low E_{OCP} values, which indicates again that the HPT-processed Zn-Mg materials are more corrosive than the other samples. This finding is comparable to the immersion test results after one week.

The characteristics of the initial corrosion behavior were investigated by PDP scans. There was a current density drop occurred in the cathodic branch at around -1.15 $V_{Ag/AgCl/NaCl}$. This is due to the anodic current increasing caused by the anodic reaction of Mg. After reaching the corrosion potential (E_{corr}), the measured current density dramatically increased, while at even higher potentials it showed a stable state due to the protection of the hydroxide film (i.e., $Zn(OH)_2$) against corrosion until the pitting corrosion potential (E_{pit}) appeared at around -0.85 $V_{Ag/AgCl/NaCl}$.

The corrosion parameters - including corrosion rate - have been determined by Tafel extrapolation. The alloys containing 1 wt % of Mg showed a higher corrosion rate than the 0.5 wt %, however, the high variation of the electrochemical test makes the results unreliable.

Therefore, the following conclusions can be drawn based on the results of this study:

- The studied Zn-Mg materials can be proposed as candidates for biodegradable medical implants applications due to their appropriate corrosion rates
- For Zn-Mg alloys, the HPT process can be applied not only to enhance the mechanical properties but also to achieve a higher corrosion rate. Here, scanning electron microscope (SEM) or electron backscatter diffraction (EBSD) methods are recommended to analyze the change in the grain boundary densities on the sample surfaces due to the HPT process.
- Due to the high variability of the PDP method, a more stable and subtle technique, such as electrochemical impedance spectroscopy (EIS), may be recommended to evaluate electrochemical corrosion properties of Zn-Mg materials.

References

[1] Shen, C. et al. (2016) ‘Mechanical properties, in vitro degradation behavior, hemocompatibility and cytotoxicity evaluation of Zn-1.2Mg alloy for biodegradable implants’, RSC advances, 6(89), pp. 8641–86419. doi:10.1039/c6ra14300h.

[2] Wong, P. et al. (2016) ‘Enhanced Mechanical Properties of MgZnCa Bulk Metallic Glass Composites with Ti-Particle Dispersion’, Metals (Basel), 6(5), p. 116. doi:10.3390/met6050116.

[3] Katarivas Levy, G., Goldman, J. and Aghion, E. (2017) ‘The Prospects of Zinc as a Structural Material for Biodegradable Implants—A Review Paper’, Metals (Basel), 7(10), p. 402. doi:10.3390/met7100402.1.2 Biodegradable materials

[4] Anderson, J.M., Rodriguez, A. and Chang, D.T. (2007) ‘Foreign body reaction to biomaterials’, Seminars in immunology, 20(2), pp. 86–100. doi:10.1016/j.smim.2007.11.004.

[5] Żwierełło, W. et al. (2020) ‘Bioelements in the treatment of burn injuries – The complex review of metabolism and supplementation (copper, selenium, zinc, iron, manganese, chromium and magnesium)’, Journal of trace elements in medicine and biology, 62, pp. 126616–126616. doi:10.1016/j.jtemb.2020.126616.

[6] Schinhammer, M. et al. (2010) ‘Design strategy for biodegradable Fe-based alloys for medical applications’, Acta biomaterialia, 6(5), pp. 1705–1713. doi:10.1016/j.actbio.2009.07.039.

[7] Peuster, M. et al. (2006) ‘Long-term biocompatibility of a corrodible peripheral iron stent in the porcine descending aorta’, Biomaterials, 27(28), pp. 4955–4962. doi:10.1016/j.biomaterials.2006.05.029.

[8] Seitz, J.-M., Lucas, A. and Kirschner, M. (2016) ‘Magnesium-Based Compression Screws: A Novelty in the Clinical Use of Implants’, JOM (1989), 68(4), pp. 1177–1182. doi:10.1007/s11837-015-1773-1.

[9] Sezer, N. et al. (2018) ‘Review of magnesium-based biomaterials and their applications’, Journal of magnesium and alloys, 6(1), pp. 23–43. doi:10.1016/j.jma.2018.02.003.

[10] Amukarimi, S. and Mozafari, M. (2021) ‘Biodegradable magnesium-based biomaterials: An overview of challenges and opportunities’, MedComm (2020), 2(2), pp. 123–144. doi:10.1002/mco2.59.

[11] Davis, J.R. (2000) Corrosion : understanding the basics /. Materials Park, OH :: ASM International, pp. 36

[12] Maret, W. and Sandstead, H.H. (2006) 'Zinc requirements and the risks and benefits of zinc supplementation', Journal of trace elements in medicine and biology, 20(1), pp. 3–18. doi:10.1016/j.jtemb.2006.01.006.

[13] Bowen, P.K. et al. (2015) 'Metallic zinc exhibits optimal biocompatibility for bioabsorbable endovascular stents', Materials Science & Engineering C, 56, pp. 467–472. doi:10.1016/j.msec.2015.07.022.

[14] Yang, H. et al. (2017) 'Evolution of the degradation mechanism of pure zinc stent in the one-year study of rabbit abdominal aorta model', Biomaterials, 145, pp. 92–105. doi:10.1016/j.biomaterials.2017.08.022.

[15] Li, H.F. et al. (2015) 'Development of biodegradable Zn-1X binary alloys with nutrient alloying elements Mg, Ca and Sr', Scientific reports, 5(1), p. 10719. doi:10.1038/srep10719.

[16] Mostaed, E. et al. (2016) 'Novel Zn-based alloys for biodegradable stent applications: Design, development and in vitro degradation', Journal of the mechanical behavior of biomedical materials, 60, pp. 581–602. doi:10.1016/j.jmbbm.2016.03.018.

[17] Zheng, Y.., Gu, X.. and Witte, F. (2014) 'Biodegradable metals', Materials science & engineering. R, Reports : a review journal, 77, pp. 1–34. doi:10.1016/j.mser.2014.01.001.

[18] Mostaed, E. et al. (2018) 'Zinc-based alloys for degradable vascular stent applications', Acta biomaterialia, 71, pp. 1–23. doi:10.1016/j.actbio.2018.03.005.

[19] Bowen, P.K., Drelich, J. and Goldman, J. (2013) 'Zinc Exhibits Ideal Physiological Corrosion Behavior for Bioabsorbable Stents', Advanced materials (Weinheim), 25(18), pp. 2577–2582. doi:10.1002/adma.201300226.

[20] Bowen, P.K. et al. (2016) 'Biodegradable Metals for Cardiovascular Stents: from Clinical Concerns to Recent Zn-Alloys', Advanced healthcare materials, 5(10), pp. 1121–1140. doi:10.1002/adhm.201501019.

[21] Haude, Michael, Prof et al. (2013) 'Safety and performance of the drug-eluting absorbable metal scaffold (DREAMS) in patients with de-novo coronary lesions: 12 month results of the prospective, multicentre, first-in-man BIOSOLVE-I trial', The Lancet (British edition), 381(9869), pp. 836–844. doi:10.1016/S0140-6736(12)61765-6.

[22] Venezuela, J. and Dargusch, M.. (2019) 'The influence of alloying and fabrication techniques on the mechanical properties, biodegradability and biocompatibility of zinc: A comprehensive review', Acta biomaterialia, 87, pp. 1–40. doi:10.1016/j.actbio.2019.01.035.

[23] Windhagen, H. et al. (2020) 'Biodegradable magnesium-based screw clinically equivalent to titanium screw in hallux valgus surgery: short term results of the first prospective, randomized, controlled clinical pilot study (vol 12, 62, 2013)', Biomedical engineering online,

19(1). doi:10.1186/s12938-020-00818-8.

[24] Stürznickel, J. et al. (2021) ‘Safety and performance of biodegradable magnesium-based implants in children and adolescents’, Injury, 52(8), pp. 2265–2271. doi:10.1016/j.injury.2021.03.037.

[25] Waizy, H. et al. (2014) ‘In vivo study of a biodegradable orthopedic screw (MgYREZr-alloy) in a rabbit model for up to 12 months’, Journal of biomaterials applications, 28(5), pp. 667–675. doi:10.1177/0885328212472215.

[26] Biber, R. et al. (2017) ‘Bioabsorbable metal screws in traumatology: A promising innovation’, Trauma case reports, 8, pp. 11–15. doi:10.1016/j.tcr.2017.01.012.

[27] McCafferty, E. (2010) Introduction to corrosion science. New York, NY [u.a.]: Springer.

[28] Liu, L. et al. (2018) ‘Initial formation of corrosion products on pure zinc in simulated body fluid’, Journal of materials science & technology, 34(12), pp. 2271–2282. doi:10.1016/j.jmst.2018.05.005.

[29] R. E. McNulty and J. D. Hanawalt 1942 Trans. Electrochem. Soc. 81 423

[30] Huang, S. et al. (2021) ‘Insight into the corrosion behavior and degradation mechanism of pure zinc in simulated body fluid’, Corrosion science, 178, p. 1.

[31] J.D. Hanawalt, C.E. Nelson, J.A. Peloubet, Transcations of the American Institute of Mining and Metallurgical Engineers (AIME), Vol 147 (1942)

[32] Dutta Majumdar, J. and Manna, I. (2013) ‘6 - Laser treatment to improve the corrosion resistance of magnesium (Mg) alloys’, in Corrosion prevention of magnesium alloys. Elsevier Ltd, pp. 135. doi:10.1533/9780857098962.2.133.

[33] Yao, C. et al. (2014) ‘Effects of Mg on microstructure and corrosion properties of Zn–Mg alloy’, Journal of alloys and compounds, 602, pp. 101–107. doi:10.1016/j.jallcom.2014.03.025.

[34] Jin, H. et al. (2018) ‘Novel high-strength, low-alloys Zn-Mg (<0.1wt% Mg) and their arterial biodegradation’, MATERIALS SCIENCE & ENGINEERING C-MATERIALS FOR BIOLOGICAL APPLICATIONS, 84, pp. 67–79. doi:10.1016/j.msec.2017.11.021.

[35] J.M. Byun, J.M. Yu, D.K. Kim, T.Y. Kim, W.S. Jung, Y.D. Kim, Corrosion behavior of Mg2Zn11 and MgZn2 single phases, Kor. J. Metal. Mater. 51 (2013) 413–419. doi:10.3365/KJMM.2013.51.6.413

[36] Prosek, T. et al. (2008) ‘Corrosion mechanism of model zinc–magnesium alloys in atmospheric conditions’, Corrosion Science, 50(8), pp. 2216–2231. doi:10.1016/j.corsci.2008.06.008.

[37] Smithells, C.J. (2004) Equilibrium diagrams. 8th ed., Smithells metals reference book. 8th ed. Amsterdam ; Boston :: Elsevier Butterworth-Heinemann, pp. 11–11–534. doi:10.1016/B978-075067509-3/50014-2.

[38] Thomas, S. et al. (2012) 'Corrosion of zinc as a function of pH', Corrosion (Houston, Tex.), 68(1), pp. 15009–15009–9. doi:10.5006/1.3676630.

[39] Meng, Y. et al. (2019) 'Initial formation of corrosion products on pure zinc in saline solution', Bioactive materials, 4(1), pp. 87–96. doi:10.1016/j.bioactmat.2018.08.003.

[40] Feliu, S., Veleva, L. and García-Galvan, F. (2019) 'Effect of Temperature on the Corrosion Behavior of Biodegradable AZ31B Magnesium Alloy in Ringer's Physiological Solution', Metals (Basel), 9(5), p. 591. doi:10.3390/met9050591.

[41] Zhang, X.G. (2011) 'Zinc', in Uhlig's Corrosion Handbook. Hoboken, NJ, USA: John Wiley & Sons, Inc, pp. 879–892. doi:10.1002/9780470872864.ch62.

[42] 'Chemical Anatomy, Physiology and Pathology of Extracellular Fluid. James L. Gamble' (1945) The Quarterly review of biology, 20(2), pp. 178–178. doi:10.1086/394820.

[43] Kokubo, T. and Takadama, H. (2006) 'How useful is SBF in predicting in vivo bone bioactivity?', Biomaterials, 27(15), pp. 2907–2915. doi:10.1016/j.biomaterials.2006.01.017.

[44] Earle, W.R., 1943. Production of malignancy in vitro. J. Natl. Cancer Inst, 4, pp.165-212.

[45] Hanks, J.H. and Wallace, R.E. (1949) 'Relation of Oxygen and Temperature in the Preservation of Tissues by Refrigeration', Proceedings of the Society for Experimental Biology and Medicine, 71(2), pp. 196–200. doi:10.3181/00379727-71-17131.

[46] Xin, Y, Hu, T & Chu, PK 2010, 'Influence of test solutions on in vitro studies of biomedical magnesium alloys', Journal of the Electrochemical Society, vol. 157, no. 7. https://doi.org/10.1149/1.3421651

[47] Liu, X. et al. (2019) 'Comparative studies of Tris-HCl, HEPES and NaHCO3/CO2 buffer systems on the biodegradation behavior of pure Zn in NaCl and SBF solutions', Corrosion science, 157, pp. 205–219. doi:10.1016/j.corsci.2019.05.018.

[48] Liu, X. et al. (2019) 'Comparative Studies on Degradation Behavior of Pure Zinc in Various Simulated Body Fluids', JOM (1989), 71(4), pp. 1414–1425. doi:10.1007/s11837-019-03357-3.

[49] Törne, K., Larsson, M., Norlin, A. and Weissenrieder, J., 2016. Degradation of zinc in saline solutions, plasma, and whole blood. Journal of Biomedical Materials Research Part B: Applied Biomaterials, 104(6), pp.1141-1151.

[50] Dong, H. et al. (2021) 'Corrosion behavior of biodegradable metals in two different

simulated physiological solutions: Comparison of Mg, Zn and Fe', Corrosion science, 182, p. 109278. doi:10.1016/j.corsci.2021.109278.

[51] Kirkland, N.., Birbilis, N. and Staiger, M.. (2012) 'Assessing the corrosion of biodegradable magnesium implants: A critical review of current methodologies and their limitations', Acta biomaterialia, 8(3), pp. 925–936. doi:10.1016/j.actbio.2011.11.014.

[52] Bowen, P.K., Drelich, J. and Goldman, J. (2013) 'Zinc Exhibits Ideal Physiological Corrosion Behavior for Bioabsorbable Stents', Advanced materials (Weinheim), 25(18), pp. 2577–2582. doi:10.1002/adma.201300226.

[53] Zhou, C. et al. (2019) 'Long-term in vivo study of biodegradable Zn-Cu stent: A 2-year implantation evaluation in porcine coronary artery', Acta biomaterialia, 97, pp. 657–670. doi:10.1016/j.actbio.2019.08.012.

[54] Yang, H. et al. (2020) 'Alloying design of biodegradable zinc as promising bone implants for load-bearing applications', Nature communications, 11(1), pp. 401–401. doi:10.1038/s41467-019-14153-7.

[55] Bowen, P.K. et al. (2015) 'Rates of in vivo (arterial) and in vitro biocorrosion for pure magnesium', Journal of biomedical materials research. Part A, 103(1), pp. 341–349. doi:10.1002/jbm.a.35179.

[56] ASTM G1-03, Standard Practice for Preparing, Cleaning, and Evaluating Corrosion Test Specimens, ASTM International, West Conshohocken, PA, 2003, www.astm.org

[57] Zhen, Z., Xi, T. and ZHENG, Y. (2013) 'A review on in vitro corrosion performance test of biodegradable metallic materials', Transactions of Nonferrous Metals Society of China, 23(8), pp. 2283–2293. doi:10.1016/S1003-6326(13)62730-2.

[58] Zhang, H. et al. (2021) 'The Effect of Immersion Corrosion Time on Electrochemical Corrosion Behavior and the Corrosion Mechanism of EH47 Ship Steel in Seawater', Metals (Basel), 11(8), p. 1317. doi:10.3390/met11081317.12

[59] Kieninger, J. (2022) Electrochemical Methods for the Micro- and Nanoscale. Berlin/Boston: Walter de Gruyter GmbH.

[60] Bard, A.J. and Faulkner, L.R. (2001) Electrochemical methods : fundamentals and applications. 2. ed.. New York, NY [u.a.]: Wiley.

[61] Srinivasan, R. and Fasmin, F. (2021) Introduction to electrochemical impedance spectroscopy. First edition.. Boca Raton :: CRC Press.

[62] Nyby, C. et al. (2021) 'Electrochemical metrics for corrosion resistant alloys', Scientific data, 8(1), pp. 58–58. doi:10.1038/s41597-021-00840-y.

[63] Bellezze, T., Giuliani, G. and Roventi, G. (2018) 'Study of stainless steels corrosion in a strong acid mixture. Part 1: cyclic potentiodynamic polarization curves examined by means of an analytical method', Corrosion science, 130, pp. 113–125. doi:10.1016/j.corsci.2017.10.012.

[64] Stern, M. and Geary, A.L., 1957. Electrochemical polarization: I. A theoretical analysis of the shape of polarization curves. Journal of the electrochemical society, 104(1), p.56.

[65] Frankel, G. S. "Wagner-Traud to Stern-Geary: development of corrosion kinetics." ; Isaacs, H.S.; Scully, J.R., Sinclair, J.D. "Corrosion science: A retrospective and current status in honor of Robert P. Frankenthal". Pennington: ECS, pp.33-41.

[66] Kokubo, T. et al. (1990) 'Solutions able to reproduce in vivo surface-structure changes in bioactive glass-ceramic A-W3', Journal of biomedical materials research, 24(6), pp. 721–734. doi:10.1002/jbm.820240607.

[67] Mueller, L. and Mueller, F.A. (2006) 'Preparation of SBF with different HCO 3 - content and its influence on the composition of biomimetic apatites', Acta biomaterialia, 2(2), pp. 181–189. doi:10.1016/j.actbio.2005.11.001.

[68] Dutta, S. et al. (2020) Experimental biotechnology : a laboratory manual /. Pitam Pura, New Delhi :: NIPA, New India Publishing Agency.

[69] Biologic 'connection to the cell': https://www.biologic.net/topics/connection-to-the-cell-part-2-multi-electrode-measurement/

[70] Reference electrode 'RE-1B' (Ag/AgCl): https://www.als-japan.com/1388.html

[71] Revie, R.W. and Uhlig, H.H. (2008) Corrosion and corrosion control : an introduction to corrosion science and engineering /. Fourth edition.. Hoboken, New Jersey :: Wiley-Interscience, a John Wiley & Sons, Inc., Publication.

[72] ASTM G102-89(1999), Standard Practice for Calculation of Corrosion Rates and Related Information from Electrochemical Measurements, ASTM International, West Conshohocken, PA, 1999, www.astm.org

[73] Popov, B.N., 2015. Corrosion engineering: principles and solved problems. Elsevier, p. 188 - 189.

[74] Pourbaix, M., (1974) Atlas of Electrochemical Equilibria in Aqueous Solutions, 2nd English edition, copyright NACE International 1974 and CEBELCOR

[75] ASTM G31-72 (1999), Standard Practice for Laboratory Immersion Corrosion Testing of Metals1, ASTM International, West Conshohocken, PA, 2020, www.astm.org

[76] ASTM G59-97(2020), Standard Test Method for Conducting Potentiodynamic Polarization Resistance Measurements, ASTM International, West Conshohocken, PA, 2020,

www.astm.org

[77] Silva, C.L.P. et al. (2019) ‘The Effect of High-Pressure Torsion on Microstructure, Hardness and Corrosion Behavior for Pure Magnesium and Different Magnesium Alloys’, Advanced engineering materials, 21(3), p. 1801081–n/a. doi:10.1002/adem.201801081.

[78] Lopes, D.R. et al. (2019) ‘Cytotoxicity and Corrosion Behavior of Magnesium and Magnesium Alloys in Hank's Solution after Processing by High-Pressure Torsion’, Advanced engineering materials, 21(8), p. 1900391–n/a. doi:10.1002/adem.201900391.

[79] Hernández-Escobar, D. et al. (2019) ‘Microstructural evolution and intermetallic formation in Zn-Mg hybrids processed by High-Pressure Torsion’, Philosophical magazine (Abingdon, England), 99(5), pp. 557–584. doi:10.1080/14786435.2018.1546962.

[80] Osório, W.R., Freire, C.M. and Garcia, A. (2005) ‘The role of macrostructural morphology and grain size on the corrosion resistance of Zn and Al castings’, Materials science & engineering. A, Structural materials : properties, microstructure and processing, 402(1), pp. 22–32. doi:10.1016/j.msea.2005.02.094.

[81] Huang, S. et al. (2021) ‘Insight into the corrosion behaviour and degradation mechanism of pure zinc in simulated body fluid’, Corrosion science, 178, p. 1. doi:10.1016/j.corsci.2020.109071.

[82] Hashimoto, M., Miyajima, S. and Murata, T. (1992) ‘A stochastic analysis of potential fluctuation during passive film breakdown and repair on iron’, Corrosion science, 33(6), pp. 885–904. doi:10.1016/0010-938X(92)90053-6.

[83] Zehetbauer, M.J. and Zhu, Y.T. (2009) Bulk Nanostructured Materials. 1. Aufl. Hoboken: Wiley-VCH. doi:10.1002/9783527626892.

[84] Aitzetmüller, L. (2021) Verfestigung biodegradierbarer ZnMg-Legierungen durch HPT-Verformung und die Auswirkung anschließender Wärmebehandlung. Master Thesis, University of Vienna, Wien.

[85] Ojdanic, A. et al. (2020) ‘The effects of severe plastic deformation and/or thermal treatment on the mechanical properties of biodegradable mg-alloys’, Metals (Basel), 10(8), pp. 1–33. doi:10.3390/met10081064.